# PMRT1, a *Plasmodium* specific parasite plasma membrane transporter is essential for asexual and sexual blood stage development

Jan Stephan Wichers[1,2,3], Paolo Mesén-Ramírez[2], Jing Yu-Strzelczyk[4], Gwendolin Fuchs[1,2,3], Jan Stäcker[2], Heidrun von Thien[1,2], Arne Alder[1,2,3], Isabelle Henshall[5], Benjamin Liffner[5], Georg Nagel[4], Christian Löw[1,6], Danny Wilson[5,7], Tobias Spielmann[2], Shiqiang Gao[4#], Tim-Wolf Gilberger[1,2,3,#], Anna Bachmann[1,2,3,&], Jan Strauss[1,2,3,6,#,&,†]

[1]Centre for Structural Systems Biology, 22607 Hamburg, Germany.
[2]Bernhard Nocht Institute for Tropical Medicine, 20359 Hamburg, Germany.
[3]Biology Department, University of Hamburg, 20146, Hamburg, Germany
[4]Institute of Physiology, Department of Neurophysiology, Biocenter, University of Wuerzburg, 97070 Würzburg, Germany
[5]Research Centre for Infectious Diseases, School of Biological Sciences, University of Adelaide, Adelaide 5005, Australia.
[6]European Molecular Biology Laboratory, Hamburg Unit, Hamburg, Germany
[7]Burnet Institute, 85 Commercial Road, Melbourne 3004, Victoria, Australia.

[#]Corresponding authors: gao.shiqiang@uni-wuerzburg.de, gilberger@bnitm.de, jan.strauss@geomar.de
[&]Contributed equally
[†]Present address: GEOMAR Helmholtz Centre for Ocean Research Kiel, 24105 Kiel, Germany

ORCID:

| | |
|---|---|
| Jan Stephan Wichers: | 0000-0002-0599-1742 |
| Paolo Mesén-Ramírez: | 0000-0001-7842-5867 |
| Jing Yu-Strzelczyk: | 0000-0002-7576-6831 |
| Gwendolin Fuchs: | 0000-0001-9294-6984 |
| Jan Stäcker: | 0000-0002-4738-6639 |
| Arne Alder: | 0000-0003-4918-4640 |
| Isabelle Henshall: | 0000-0002-5906-0687 |
| Benjamin Liffner: | 0000-0002-1573-6139 |
| Danny Wilson: | 0000-0002-5073-1405 |
| Georg Nagel: | 0000-0001-8174-8712 |
| Christian Löw: | 0000-0003-0764-7483 |
| Tobias Spielmann: | 0000-0002-3968-4601 |
| Shiqiang Gao: | 0000-0001-6190-9443 |
| Tim-Wolf Gilberger: | 0000-0002-7965-8272 |
| Anna Bachmann: | 0000-0001-8397-7308 |
| Jan Strauss: | 0000-0002-6208-791X |

**Abstract**

Membrane transport proteins perform crucial roles in cell physiology. The obligate intracellular parasite *Plasmodium falciparum*, an agent of human malaria, relies on membrane transport proteins for the uptake of nutrients from the host, disposal of metabolic waste, exchange of metabolites between organelles and generation and maintenance of transmembrane electrochemical gradients for its growth and replication within human erythrocytes. Despite their importance for *Plasmodium* cellular physiology, the functional roles of a number of membrane transport proteins remain unclear, which is particularly true for orphan membrane transporters that have no or limited sequence homology to transporter proteins in other evolutionary lineages. Therefore, in the current study, we applied endogenous tagging, targeted gene disruption, conditional knockdown and knockout approaches to investigate the subcellular localization and essentiality of six membrane transporters during intraerythrocytic development of *P. falciparum* parasites. They are localized at different subcellular structures – the food vacuole, the apicoplast, and the parasite plasma membrane – and showed essentiality of four out of the six membrane transporters during asexual development. Additionally, the plasma membrane resident transporter 1 (PMRT1, PF3D7_1135300), a unique *Plasmodium*-specific plasma membrane transporter, was shown to be essential for gametocytogenesis. Heterologous expression of wild-type and mutation constructs in *Xenopus laevis* oocytes indicated ion transport upon membrane hyperpolarization and a functional role of negatively charged amino acids protruding into the parasitophorous vacuole lumen. Overall, we reveal the importance of four orphan transporters to blood stage *P. falciparum* development and provide the first functional characterization of *Pf*PMRT1, an essential parasite membrane transporter.

**Importance (150 words)**

*Plasmodium falciparum*-infected erythrocytes possess multiple compartments with designated membranes. Transporter proteins embedded in these membranes do not only facilitate movement of nutrients, metabolites and other molecules between these compartments, but are common therapeutic targets and can also confer antimalarial drug resistance. Orphan membrane transporter in *P. falciparum* without sequence homology to transporters in other evolutionary lineages and distant to host transporters may constitute attractive targets for novel intervention approaches. Here, we localized six of these putative transporters at different subcellular compartments and probed into their importance during asexual parasite growth using reverse genetic approaches. In total, only two candidates turned out to be dispensable for the parasite, highlighting four candidates as putative targets for therapeutic interventions. This study reveals the importance of several orphan transporters to blood stage *P. falciparum* development and provides the first functional characterization of *Pf*PMRT1, an essential parasite membrane transporter.

## Introduction

*Plasmodium* spp. malaria parasites inhabit diverse intracellular niches and need to import nutrients and export waste across both, host-cell and parasite membranes. Despite this, there are less than 150 putative membrane transporters encoded in the genome of *Plasmodium falciparum*, the most virulent malaria parasite, making up only 2.5% of all encoded genes (*P. falciparum* 3D7 v3.2: 5280 genes) (1–5), which is reduced compared to other unicellular organisms of similar genome size. The loss of redundant transporters is a typical feature of many intracellular parasites (6) and, as a result, the proportion of transporters that are indispensable for parasite survival increases (2), some of which have been shown to be critical for the uptake of several anti-Plasmodial compounds and/or to be involved in drug resistance (7–20). Moreover, the parasite's intracellular lifestyle resulted in the evolution of additional specialized transporters without human homologues (1). During its intraerythrocytic development, the parasite relies on the uptake of nutrients, such as amino acids, pantothenate or fatty acids, from its host erythrocyte as well as from the extracellular blood plasma (21–24). As *P. falciparum* resides in a parasitophorous vacuole (PV) in the host erythrocyte, nutrients acquired from the extracellular milieu must traverse multiple membranes: the erythrocyte plasma membrane (EPM), the parasitophorous vacuole membrane (PVM), the parasite plasma membrane (PPM) and eventually membranes of intracellular organelles, such as those of the apicoplast or mitochondria (21, 25–27). The unique requirements of malaria parasite survival have led to the evolution of a number of orphan transporters, whose localization or function cannot be predicted based on sequence homology to transporters in other organisms (4, 28). Despite the likely importance of uniquely adapted transporters to *P. falciparum* survival, subcellular localization, essentiality, function and substrate specificity for most *P. falciparum* transporters has not been directly determined (2, 21, 26). The best functional evidence available for many *Plasmodium*-specific transporters comes from a recent knockout screen of these orphan transporters in the rodent malaria parasite *Plasmodium berghei* (28). However, whether observations for different transporters in the *P. berghei* model are directly transferrable to *P. falciparum* have yet to be examined. Therefore, in this study, we explored the localization and essentiality of four predicted orphan transporters that had been partially characterised in *P. berghei* and included two additional transporters with no experimental characterization available.

## Results

A subset of orphan transporters characterized in the *P. berghei* malaria model was selected for further characterization in *P. falciparum*. The four transporters selected were reported to be important at different stages of rodent malaria parasite growth with i) *P. berghei* drug/metabolite transporter 2 (*Pf*DMT2: PF3D7_0716900) found to be essential for asexual blood stage development, ii) *P. berghei* zinc transporter 1 (*Pf*ZIP1: PF3D7_0609100) was

essential across transmission stages but not blood stages, where there was only a slight growth defect, iii) *P. berghei* cation diffusion facilitator family protein (*Pf*CDF: PF3D7_0715900) knockout parasites had a defect during transmission stages but not during asexual stages, and iv) *P. berghei* major facilitator superfamily domain-containing protein (*Pf*MFS6: PF3D7_1440800) was found to be essential for parasite transmission from mosquitos to a new host, with a growth defect observed at asexual and gametocyte stages but not during mosquito stage parasite growth (28, 29). In order to confirm expression of these transporters in *P. falciparum* asexual stages, we screened the list of "Genes coding for transport proteins" included in the Malaria Parasite Metabolic Pathways (MPMP) database (1, 30) for proteins with i) RNA-seq (31, 32) and ii) proteomics evidence (33, 34) for expression in asexual blood stages. We identified two additional putative transporters (PF3D7_0523800, PF3D7_1135300) which had yet to be functionally characterized in the *P. berghei* screen by Kenthirapalan *et al.* (28) or any other experimental model. Both were subsequently included in our characterization of *P. falciparum* orphan transporters, and named as 'food vacuole resident transporter 1' (FVRT1: PF3D7_0523800) and as 'plasma membrane resident transporter 1' (PMRT1: PF3D7_1135300) based on their subcellular localization. AlphaFold-based structure predictions (35) and results from structure homology search (36) of all six selected transporters are provided in Figure S1.

**Localization of putative *P. falciparum* transporters**

To determine subcellular localization, we tagged the six putative transporters endogenously with GFP using the selection-linked integration (SLI) system (37) (Figure 1A). Additionally, a glmS ribozyme sequence was included in the 3'UTR, which enabled conditional gene knockdown upon addition of glucosamine (38). Correct integration of the plasmid into the respective genomic locus was verified by PCR and expression of the GFP-fusion protein was confirmed by Western blot for each generated cell line (Figure S2A, B).

All transgenic cell lines expressed the GFP-fusion protein, demonstrating that these transporters are expressed in asexual blood stage parasites (Figure 1B-G, S2A). Expression levels were sufficient to allow determination of subcellular localization (Figure 1B–G): (i) PF3D7_0523800-GFP localized to the food vacuole, (ii) *Pf*DMT2-GFP and *Pf*MFS6-GFP apicoplast localization, and (iii) *Pf*ZIP1-GFP and PF3D7_1135300-GFP parasite plasma membrane (PPM) localization. However, *Pf*CDF-GFP showed an obscure staining pattern with a weak spot within the parasite cytosol in ring and trophozoite state parasites, but multiple foci in schizont stages (Figure 1D). To pinpoint this localization, an additional cell line with endogenously 3xHA-tagged *Pf*CDF was generated, confirming the focal localization of *Pf*CDF in asexual stages (Figure S2C).

Except for *Pf*CDF, the observed localizations of the other five transporters were confirmed by co-localization studies using appropriate episomally expressed marker proteins: P40PX-

mCherry (39, 40) for the food vacuole, ACP-mCherry (41, 42) for apicoplast and Lyn-mCherry (37, 43) for PPM. The focal distribution of *Pf*CDF-GFP was co-localized with a rhoptry (ARO-mCherry (44, 45)) and a micronemes (AMA1-mCherry (46, 47)) marker, but *Pf*CDF-GFP did not colocalize with either marker (Figure 1H). Additionally, for *Pf*ZIP and PF3D7_1135300 the PPM localization was further confirmed in free merozoites (Figure S2D, E). Accordingly, as noted above, we named PF3D7_0523800 as 'food vacuole resident transporter 1' (FVRT1) and PF3D7_1135300 as 'plasma membrane resident transporter 1' (PMRT1).

**Targeted-gene disruption (TGD), conditional knockdown and conditional knockout of putative transporters**

In order to test whether the putative transporters are essential for *P. falciparum* during its intraerythrocytic cycle, we first tried to functionally inactivate them by targeted gene disruption (TGD) using the SLI system (37) (Figure S3A). TGD cell lines were successfully obtained for *Pf*ZIP1 and *Pf*CDF (Figure S3B, C). For *Pf*ZIP1-TGD, the correct integration of the plasmid into the genomic locus and absence of wildtype locus was verified by PCR and subsequent growth experiments revealed no growth defect compared to *P. falciparum* 3D7 wildtype parasites (Figure S2B), suggesting its redundancy during asexual parasite proliferation. For *Pf*CDF-TGD the correct integration of the plasmid into the genomic locus was also verified, but wildtype DNA was still detectable and remained even upon prolonged culturing under G418/WR selection and limited dilution cloning (Figure S3C). In contrast, six (*Pf*PMRT1, *Pf*DMT2) or eight (*Pf*FVRT1, *Pf*MFS6) independent attempts to obtain TGD cell lines for the other four transporters with the respective plasmids failed, indicating that these genes have an indispensable role in blood stage parasite growth.

To probe into the function of the putative transporters where we were unable to generate gene-knockout parasites, we utilized the glmS ribozyme sequence. The corresponding sequence was integrated into the 3'UTR of the targeted genes. This enabled the induction of conditional degradation of respective mRNAs upon addition of glucosamine (38) and the assessment of the phenotypic consequences. Upon addition of 2.5 mM glucosamine to young ring stage parasites we found a 76.8% (+/- SD 3.7) reduction in GFP fluorescence intensity in *Pf*DMT2-GFP parasites, 72.7% (+/- SD 9.4) reduction in *Pf*MFS6-GFP and a 77.7% (+/- SD 6.1) reduction in *Pf*PMRT1-GFP in schizonts of the same cycle (Figure 2A–C, S4A–C). No measurable reduction in fluorescence intensity could be detected for *Pf*FVRT1-GFP or *Pf*CDF-GFP expressing parasite lines (Figure S4D–F). For parasite cell lines with a significant reduction in the expression of the endogenously tagged protein, proliferation was analyzed in the absence and presence of 2.5 mM glucosamine (Figure 2D, S4G). While no significant effect on growth was observed for *Pf*MFS6 and *Pf*PMRT1, a growth reduction of 68.5 % (+/- SD 2.1) over two cycles was observed upon knockdown of *Pf*DMT2. For *Pf*PMRT1, a minor growth delay was measurable, which resulted in a reduced parasitemia at day 3 upon knockdown

using both, 2.5 mM or 5 mM glucosamine (Figure 2E), and fewer newly formed ring stage parasites at 84 hours post invasion (hpi) (Figure 2F) were observed.

To better characterize the minor growth phenotype of *Pf*PMRT1-GFP-glmS parasites that might be due to incomplete knockdown, we generated a conditional *Pf*PMRT1 knockout cell line (condΔPMRT1) using the Dimerizable Cre (DiCre) system (48, 49). Again using the SLI system (37), the endogenous *Pf*PMRT1 was disrupted upstream of the region encoding the N-terminal transmembrane domain, but, at the same time introducing a recodonized second functional copy of *Pf*PMRT1 flanked by loxP sites in the genomic locus. This loxP-flanked allelic copy of *Pf*PMRT1 encodes an additional 3x hemagglutinin (HA) tag, which can be conditionally excised upon addition of a rapamycin analog (rapalog) via the enzymatic activity of an episomally expressed DiCre (Figure 3A). First, correct integration of the plasmid into the genomic locus was verified by PCR (Figure 3B). Second, expression and localization of the recodonized HA-tagged protein at the PPM was verified by colocalization with the merozoite plasma membrane marker MSP1 (50) (Figure 3C). Third, excision of the recodonized gene upon rapalog addition was confirmed on genomic level by PCR (Figure 3D) and on protein level by Western blot analysis at 24 hpi and 48 hpi (Figure 3E). To assess the effect of conditional *Pf*PMRT1 knockout on parasite proliferation, we determined growth of the transgenic parasite cell line with and without rapalog over five days (Figure 3F, S5A). In contrast to the glmS-based knockdown experiment, DiCre-based gene excision (induced by the addition of rapalog to young ring stages of condΔPMRT1 parasite cell cultures) abolished growth within the first replication cycle (Figure 3F, S5A). The specificity of the observed growth phenotype was verified by gene complementation. To achieve this, we episomally expressed recodonized *Pf*PMRT1 with TY1-epitope tag either under the constitutive *nmd3* or the weaker *sf3a2* promoter (51) in the condΔPMRT1 cell line (Figure 3D, F, S5B, C). Correct localization of the TY1-tagged *Pf*PMRT1 at the PPM was verified by immunofluorescence assays (IFA) (Figure 3G). Notably both, complementation of the *Pf*PMRT1 knockout cell line (condΔPMRT1) with recodonized *Pf*PMRT1 either under control of the constitutive *nmd3* or the weaker *sf3a2* promoter, restored parasite growth (Figure 3F, S5B, C). The level of growth restoration with low level expression of recodonized *Pf*PMRT1 is in line with the results from glmS-knockdown experiments, which showed that a reduction of about 75% in protein expression resulted only in a minor growth perturbation (Figure 2C, D).

**Loss of the PPM-localized *Pf*PMRT1 leads to an arrest of parasite development at trophozoite stage and the formation of vacuoles**

To determine, which particular parasite stages are affected by the knockout of *Pf*PMRT1, we added rapalog to tightly synchronized parasites at different time points (4, 20 and 32 hpi) (Figure 4A) and monitored parasite growth by flow cytometry. Additionally, we quantified growth perturbation by microscopy of Giemsa smears at 4, 20, 24, 32, 40, 48, 72 and 96 hpi

(Figure 4B, S6A, B). When adding rapalog at 4 hpi, parasite development progressed through ring and early trophozoite stages up to 24 hpi with no visible abnormality. Afterwards, parasites with deformed and enlarged vacuoles started to appear and further development occurred to be stalled. At 32 hpi, almost all parasites had developed to late trophozoites/early schizonts in the control, whereas these stages were completely absent in *Pf*PMRT1-deficient parasites. Over 50% of the parasites were pycnotic or possessed large vacuoles, the remaining parasites stayed arrested at the trophozoite stage. Quantification of the percentage of parasites with vacuoles between 20 hpi and 32 hpi revealed 94.8% (+/- SD 4.0) vacuole-positive parasites (Figure 4C). The activation of gene excision at later time points by adding rapalog at 20 hpi or 32 hpi resulted in no or minor growth perturbation in the first cycle with successful re-invasion, but again led to parasites arresting at the trophozoite stage in the second cycle with an accumulation of vacuoles (Figure 4A, S6A, B).

In order to get further insights into the morphological changes in *Pf*PMRT1-deficient parasites with its vacuolization, we incubated these parasites with dihydroethidium (DHE) to visualize the parasite cytosol (40). We observed an absence of staining in the vacuoles, suggesting they are not filled with parasite cytosol (Figure 4D). Next, we transfected the condΔPMRT1 cell line with a plasmid encoding the PPM marker Lyn-mCherry (37) and observed Lyn-mCherry-positive vacuoles upon knockout of *Pf*PMRT1 starting to become visible at 24 hpi, indicating that the vacuoles originate from the PPM (Figure 4E). In line with this, vacuole membranes were also stainable with BODIPY TR C5 ceramide in condΔPMRT1 parasites at 32 hpi (Figure 4F).

**Depletion of *Pf*PMRT1 results in an early arrest of gametocyte development**

RNA-seq data suggest *Pf*PMRT1 is also expressed during other developmental stages, such as gametocytes (52, 53). Therefore, we assessed expression of *Pf*PMRT1-GFP during gametocytogenesis by re-engineering *Pf*PMRT1-GFP-glmS in the inducible gametocyte producer (iGP) '3D7-iGP (55)' parasite line, which allows the robust induction of sexual commitment by conditional expression of gametocyte development 1 protein (GDV1) upon addition of shield-1 (55) (Figure S7A). We show that *Pf*PMRT1 is indeed expressed during all stages of gametocytogenesis and again localizes to the PPM, colocalizing with the PPM-marker Lyn-mCherry (37) (Figure 5A, B). Conditional knockdown of *Pf*PMRT1 via the glmS-ribozyme system (Figure S7B) resulted in a reduction in *Pf*PMRT1-GFP fluorescence intensity of 79.4% (+/- SD 9.2%) at 7 days post induction (dpi) or 75.5% (+/- SD 23.2%) at 10 dpi, without an effect on gametocyte development (Figure S7C–F). In order to exclude that a role of *Pf*PMRT1 in gametocytogenesis is covered by only a partial knockdown resulting in low levels of expressed protein and to determine if *Pf*PMRT1 is essential for gametocytogenesis, we episomally expressed GDV1-GFP-DD in the condΔPMRT1 parasite line, enabling conditional induction of sexual commitment upon addition of shield 1 in these parasites (56). Conditional

knockout of *Pf*PMRT1 in these transgenic parasites at day three post gametocyte induction resulted in pycnotic parasites from day 5 onwards, while excision of *Pf*PMRT1 at day 5 post induction had no effect on gametocyte development (Figure 5C, D). Excision of the recodonized gene upon rapalog addition was confirmed at a genomic level by PCR for both conditions (Figure 5E). Quantification of parasite stages at day 10 post induction of GDV1 expression revealed 77.9% (+/- SD 7.7%) gametocytes and 22.1% (+/- SD 7.7%) pycnotic parasites in the control, while 100% of parasites were already pycnotic in the cultures, with induced knockout by addition of rapalog at day 3 post gametocyte induction by GDV1 expression (Figure 5F). This data indicates that *Pf*PMRT1 is important for early gametocyte development.

**PMRT1 is unique to the genus *Plasmodium* and interspecies complementation assays showed partial functional conservation**

*Pf*PMRT1 shows a lack of sequence similarities with known or putative transporters and/or conserved domains shared with known transporter families (2, 5). Our phylogenetic analysis revealed that homologs of *Pf*PMRT1 are present across *Plasmodium* species with amino acid sequence identities of about 90% in the subgenus *Laverania*, but about 50% outside *Laverania* (Figure 6A). However, prediction of the protein structure using AlphaFold (35) indicates two bundles of four transmembrane helices with reasonable similarity of the C-terminal bundle with the photosynthetic reaction center Maquette-3 protein (57) (RMSD of 3.12) (Figure 6B, Figure S1B). In order to test for functional conservation, we expressed the *Pf*PMRT1 homologs of *P. vivax* (PVP01_0936100) and *P. knowlesi* (PKNH_0933400) episomally as C-terminal Ty-1 fusion proteins under the *nmd3* promoter in the condΔPMRT1 parasites. Both protein variants localized correctly at the PPM, as shown by IFA (Figure 6C), and were able to partially restore growth after two cycles to 64.8% (+/- SD 9.8%) and 65.1% (+/- SD 7.4%) compared to the control (Figure 6D, S8). Excision of the recodonized endogenous *Pfpmrt1* gene upon rapalog addition was confirmed at a genomic level by PCR (Figure 6E). These data indicate that PMRT1 is functionally conserved within the genus *Plasmodium*.

**Functional characterization of *Pf*PMRT1 in *Xenopus* oocytes revealed hyperpolarization-activated ion transport activity**

*Pf*PMRT1 encodes a 410 amino acid protein with eight predicted (58) transmembrane domains (TM) (Figure S1). The N- and C-terminal parts of *Pf*PMRT1 are both predicted (59) to be facing the cytosolic side of the parasite. Surface electrostatics indicate a clear polarity of *Pf*PMRT1 with negative charges facing the parasitophorous vacuole (PV) lumen and positive charges inside the parasite cytosol (Figure 7A). The loops protruding into the PV lumen of *Pf*PMRT1 are generally larger than the cytosolic loops and possess several negatively charged amino acids, especially the first loop between TM1 and TM2 with 10 negatively charged amino acids.

In contrast, the loop between TM4 and TM5 on the parasite cytosol (PC) side contains six positively charged amino acids. These two stretches of charged amino acids were hypothesized to be important for protein function and were replaced with neutral amino acids to test this hypothesis (Figure 7B). Full-length, WT *Pf*PMRT1 as well as the two mutants (MutPV, with sequence **EDD**I**DE**YNIKGN**EEE** modified to **QNA**I**AQ**YNIKGN**AAA**; MutPC, with sequence **K**I**EKH**F**RKK**F modified to **A**I**QAA**F**AMA**F), each as C-terminal eYFP fusion proteins, were expressed in *Xenopus laevis* oocytes in order to characterize its function (Figure 7D). The *Pf*PMRT1-WT expressing oocytes showed significant inward currents when clamped at -160 mV, indicating a hyperpolarization-activated ion transport (Figure 7C). The current of MutPV-expressing oocytes was significantly reduced compared to *Pf*PMRT1-WT ($W$ = 10, $n_1$ = 10, $n_2$ = 7, $P$ = 0.0147, two tailed Wilcoxon rank sum test), while in MutPC-expressing oocytes the observed current was only slightly smaller than in WT controls (Figure 7D, E), suggesting that the negatively charged amino acids of the first loop protruding into the PV lumen are important for the function of *Pf*PMRT1. To translate these results to the parasite, we expressed *Pf*PMRT1-WT and the two sequence mutants as C-terminal Ty-1 fusion complementation constructs under the *nmd3* promoter in cond*Δ*Pf*PMRT1 parasites. These experiments showed, that *Pf*PMRT1-MutPC was able to completely restore parasite growth, while *Pf*PMRT1-MutPV showed only 59.2% (SD +/- 9.5) growth compared to the control after two developmental cycles (Figure 7F, G, S9 A–C). These data support the functional role of the negatively charged amino acids of the first loop protruding into the parasitophorous vacuole lumen for transport activity during the intraerythrocytic developmental cycle of the parasite.

## Discussion

To date, the predicted 'transportome' of *P. falciparum* consists of 117 putative transport systems (encoded by 144 genes) classified as channels (n=19), carriers (n=69), and pumps (n=29) (2). Functions of the vast majority of transporter genes were inferred from sequence homology to model organisms, however, given their lack of homology, 39 gene products could not be associated with any functional or subcellular localization and were categorized as orphan transporters accordingly (4). Here, we concentrated on four candidates from the orphan group, which were already partially characterized in *P. berghei*, and included two additional so far uncharacterized putative transporter proteins.

We localized *Pf*FVRT1-GFP – annotated on PlasmoDB (60) as putative divalent metal transporter – at the food vacuole of the parasite, which is in line with a previously predicted food vacuole association (1) and its reported homology (1, 61) to the conserved eukaryotic endosomal/lysosomal natural resistance-associated macrophage protein (NRAMP) transporter (62) in our structure similarity search. Repeated attempts to generate a TGD cell line failed, indicating an important role of this transporter during asexual blood stage

development which is in agreement with data from a *P. falciparum* genome wide essentiality screen (63).

In concordance with recently published data identifying *Pb*DMT2 and *Pb*MFS6 as leaderless apicoplast transporters (29), we localized GFP-fusion proteins of *Pf*DMT2 and *Pf*MFS6 at the apicoplast. Successful knockdown of *Pf*DMT2 resulted in a growth defect in the second cycle after induction, resembling the described delayed death phenotype of other apicoplast genes that were functionally inactivated (29, 64–66). It suggests an essential role of *Pf*DMT2 in apicoplast physiology, as observed by Sayers *et al.* (29) for the rodent malaria *P. berghei*. This is further supported by our failed attempts to disrupt this gene using the SLI system.

We also failed to disrupt the *Pf*MFS6 locus, which is in agreement with the gene knockout studies in *P. berghei* that led to a markedly decreased multiplication rate (28, 29, 67). Nevertheless, glmS-based knock-down, although comparable to *Pf*DMT2-GFP knockdown (72.7% versus 76.8% reduction in GFP fluorescence, respectively) had no effect on parasite proliferation in our study. This might indicate that these reduced levels of *Pf*MFS6, in contrast to reduced levels of *Pf*DMT2, are sufficient for normal asexual replication *in vitro*.

Another candidate, *Pf*CDF, annotated as putative cation diffusion facilitator family protein, showed multiple cytosolic foci within the parasite with no co-localization with apical organelle markers. The homologue in *Toxoplasma gondii*, *Tg*ZnT (TgGT1_251630) shows a similar cellular distribution (68). It has recently been shown to transport $Zn^{2+}$, to localize to vesicles at the plant-like vacuole in extracellular tachyzoites and to be present at dispersed vesicles throughout the cytoplasm of intracellular tachyzoites (68). Our data suggests that *Pf*CDF is not essential for parasite *in vitro* blood stage development even though we were not able to generate a clonal wild-type free TGD cell line. Its redundancy is further supported by published data, showing that CDF proteins are non-essential for *in vivo* blood stage development in *P. yoelli* (69) *and P. berghei* (28, 67) and by its high (1.0) mutagenesis index score in a *P. falciparum* genome-wide mutagenesis screen (63).

Finally, two putative transporters, *Pf*ZIP1 and *Pf*PMRT1, localized to the PPM. We show that *Pf*ZIP1 is non-essential for *P. falciparum in vitro* blood stage development, in line with a high (0.7) mutagenesis index score in a *P. falciparum* genome-wide mutagenesis screen (63). However, this is in contrast to the reported strong fitness loss in *P. berghei* (67) knockout mutants and failed knockout attempts in *P. yoelli* and *P. berghei in vivo* mouse models (29, 69). These observations may reflect differences between *Plasmodium* species or differing requirements for *in vitro* and *in vivo* growth conditions.

*Pf*PMRT1 is annotated as a conserved *Plasmodium* membrane protein with unknown function. It has been described as a protein showing structural characteristics of a transporter, without sharing sequence similarities with known or putative transporters and/or conserved domains of known transporter families (2, 5). Our phylogenetic analysis confirmed PMRT1 as unique

for *Plasmodium* species with high sequence conservation only within the *Laverania* subgenus (70). In line with data from genome-wide mutagenesis screens (63, 67) and reported failed knockout attempts in *P. yoelli* (69), we found that *Pf*PMRT1 is essential for parasite growth, as its functional inactivation resulted in growth arrest at the trophozoite stage accompanied by the accumulation of PPM-derived vacuoles within the parasite. In contrast, conditional knockdown resulted only in a growth delay, indicating that minor residual *Pf*PMRT1 protein levels appear to be sufficient to promote parasite growth. This finding was validated by episomal expression of an allelic copy under the control of the weak *sf3a2* promoter (51) in the *Pf*PMRT1 knockout parasites. Additionally, we found that *Pf*PMRT1 is essential for early gametocytogenesis. Interestingly, the induction of the knockout at stage II–III had no effect on gametocytogenesis. This might be due to sufficient amounts of *Pf*PMRT1 already present at the PPM, but could also indicate that the function of the transporter is not required for later stage gametocyte maturation.

The *Pf*PMRT1-WT-expressing *Xenopus* oocytes showed a hyperpolarization-activated ion transport activity, which is reduced in the variant featuring mutations in the first loop that extends into the parasitophorous vacuole. But it remains to be determined whether the hyperpolarization-activated ion transporting activity is the main physiological function of *Pf*PMRT1. Additional functions such as transporting of other molecules, or cooperative interaction with other parasite proteins might play a role under physiological conditions. However, the mutation analysis suggested that the negatively charged amino acids of the first loop protruding into the PV lumen are important for the function of *Pf*PMRT1. Interestingly, AlphaFold predicts smaller helical structures within this negatively charged loop, which possibly function as flexible gates and/or could be involved substrate binding.

For future work, further functional and pharmacological characterization of this transporter will provide insights into its biological role in different stages of the parasites life cycle, as transcriptomic data indicates – along with expression in blood stages (31, 32) – *Pf*PMRT1 is expressed in oocysts of *P. falciparum* (54, 71) and *P. berghei* (72).

## Material and methods

### Cloning of plasmid constructs for parasite transfection

For endogenous tagging using the SLI system (37) a 889 bp (for *Pf*PMRT1; PF3D7_1135300), 905 bp (*Pf*FVRT1; PF3D7_0523800), 827bp (*Pf*ZIP1; PF3D7_0609100), 873 bp (*Pf*DMT2; PF3D7_0716900), 877 bp (*Pf*MFS6; PF3D7_1440800), 785 bp (*Pf*CDF; PF3D7_0715900) long homology region (HR) was amplified using 3D7 gDNA and cloned into pSLI-GFP-glmS (73) (derived from pSLI-GFP (37)) using the NotI/MluI restriction site. In order to generate

*Pf*PMRT1-2xFKBP-GFP a 1000 bp long HR was amplified using 3D7 gDNA and cloned into pSLI-2xFKBP-GFP (37).

For SLI-based targeted gene disruption (SLI-TGD) (37) a 501 bp (*Pf*PMRT1), 378 bp (*Pf*FVRT1), 511 bp (*Pf*ZIP1), 399 bp (*Pf*DMT2), 396 bp (*Pf*MFS6), 741 bp (*Pf*CDF) long homology region was amplified using 3D7 gDNA and cloned into the pSLI-TGD plasmid (37) using NotI and MluI restriction sites.

For conditional deletion of *Pf*PMRT1, the first 492 bp of the *Pf*PMRT1 gene were PCR amplified to append a first loxP site and a recodonized T2A skip peptide. The recodonized full-length coding region of *Pf*PMRT1 was synthesized (GenScript, Piscataway, NJ, USA) and PCR amplified with primers to add a second loxP site after the gene to obtain a second fragment. Both fragments were cloned into pSLI-3xHA (51), using NotI/SpeI and AvrII/XmaI sites. This resulted in plasmid pSLI-*Pf*PMRT1-loxP and the resulting transgenic cell line after successful genomic modification was transfected with pSkip-Flox (37) using 2 µg/ml Blasticidin S to obtain a line expressing the DiCre fragments (cond∆PMRT1).

For complementation constructs, the recodonized *Pf*PMRT1 gene was PCR amplified using primers to append the TY1 sequence and cloned via XhoI and AvrII or KpnI into pEXP1comp (51) containing yDHODH as a resistance marker and different promoters (*nmd3 (*PF3D7_0729300), *sf3a2 (*PF3D7_0619900)) driving expression of the expression cassette. This resulted in plasmids c-$^{nmdr}$*Pf*PMRT1-ty1 and c-$^{sf3a2}$*Pf*PMRT1-ty1.

*Pf*PMRT1 homologues of *P. vivax (*PVP01_0936100) (74) *and P. knowlesi (*PKNH_0933400) (75) were amplified from parasite gDNA and cloned into p$^{nmd3}$EXP1comp (51) via the XhoI/AvrII restriction site. For co-localization experiments the plasmids pLyn-FRB-mCherry (37), P40PX-mCherry (40), pARL-$^{crt}$ACP-mCherry (42), pARL-$^{ama1}$ARO-mCherry (44) and pARL-$^{ama1}$AMA1-mCherry (47) were used. For conditional gametocyte induction yDHODH was amplified by PCR from pARL-$^{ama1}$AMA1-mCherry-yDHODH (47) and cloned into GDV1-GFP-DD-hDHFR(56)(56) using the XhoI/XhoI restriction site. For expression in Xenopus oocysts *Pf*PMRT1 was amplified from c-$^{nmdr}$*Pf*PMRT1-ty1 and DNA fragments were ligated and inserted into the oocyte expression vector pGEM-HE (76), containing a C-terminal eYFP using the BamHI/XhoI restriction site. As a control of plasma membrane-targeted channel protein, the cyclic nucleotide-gated potassium channel SthK (77) was also cloned into the pGEM-HE vector with C-terminal eYFP using the BamHI/XhoI restriction site.

The pGEM-HE plasmids containing SthK, *Pf*PMRT1 or the mutant were linearized by NheI digestion before the RNA generation. Mutations were made by QuikChange Site-Directed Mutagenesis. The complementary RNA (cRNA) was synthesized by in vitro transcription using the AmpliCap-MaxT7 High Yield Message Maker Kit (Epicentre).

Sequences of the MutPC and MutPV variants were amplified from pGEM plasmid constructs and cloned into c-$^{nmd3}$*Pf*PMRT1-ty1 using the XhoI/AvrII restriction site.

Oligonucleotides and plasmids used in this study are listed in Table S1A and S1B.

**_P. falciparum_ culture and transfection**

Blood stages of *P. falciparum* 3D7 were cultured in human erythrocytes (O+). Cultures were maintained at 37°C in an atmosphere of 1% $O_2$, 5% $CO_2$ and 94% $N_2$ using RPMI complete medium containing 0.5% Albumax according to standard protocols (78). To maintain synchronized parasites, cultures were treated with 5% sorbitol (79).

Induction of gametocytogenesis was done as previously described (55, 56). Briefly, GDV1-GFP-DD expression was achieved by addition of 4 µM shield-1 to the culture medium and gametocyte cultures were treated with 50 mM N-acetyl-D-glucosamine (GlcNAc) for five days starting 72 hours post shield-1 addition to eliminate asexual parasites(80). Alternatively, asexual ring stage cultures with >10% parasitemia were synchronized with Sorbitol (79) cultured for 24 hours and treated with 50 mM N-acetyl-D-glucosamine (GlcNAc) (80) for five days.

For transfection, Percoll-purified (81) late-schizont-stage parasites were transfected with 50 µg of plasmid DNA using Amaxa Nucleofector 2b (Lonza, Switzerland) as previously described(82). Transfectants were selected either using 4 nM WR99210 (Jacobus Pharmaceuticals), 2 µg/ml Blasticidin S (Life Technologies, USA), or 0.9 µM DSM1 (83) (BEI Resources; https://www.beiresources.org). In order to select for parasites carrying the genomic modification using the SLI system (37), G418 (Sigma-Aldrich, St. Louis, MO) at a final concentration of 400 µg/ml was added to 5% parasitemia culture. The selection process and testing for integration were performed as previously described (37).

For SLI-TGD, a total of six (*Pf*PMRT1, *Pf*DMT2, *Pf*ZIP1, *Pf*CDF) or eight (*Pf*FVRT1, *Pf*MFS6) independent 5 ml cultures containing the episomal plasmid were selected under G418 for at least eight weeks.

**Imaging and immunofluorescence analysis (IFA)**

Images of *Xenopus* oocysts were taken 3 days after injection using a Carl Zeiss LSM 5 Pascal Laser Scanning Confocal Microscope, with a 40x/0.8 water immersion objective. The eYFP fluorescence was excited at 514 nm of the Argon laser and obtained at 530 - 600 nm.

Fluorescence images of infected erythrocytes were observed and captured using a Zeiss Axioskop 2plus microscope with a Hamamatsu Digital camera (Model C4742-95), a Leica D6B fluorescence microscope equipped with a Leica DFC9000 GT camera and a Leica Plan Apochromat 100x/1.4 oil objective or an Olympus FV3000 with a x100 MPLAPON oil objective (NA 1.4).

Microscopy of unfixed IEs was performed as previously described (84). Briefly, parasites were incubated in RPMI1640 culture medium with Hoechst-33342 (Invitrogen) for 15 minutes at 37°C prior to imaging. 7 µl of IEs were added on a glass slide and covered with a cover slip.

BODIPY TR C5 ceramide (Invitrogen) staining was performed by adding the dye to 32 hours post invasion parasites in a final concentration of 2.5 µM in RPMI as previously described (84). For DHE staining of the parasite cytosol (40), 80 µl of resuspended parasite culture were incubated with DHE at a final concentration of 4.5 µg/ml in the dark for 15 minutes prior to imaging.

IFAs were performed as described previously (85). Briefly, IEs were smeared on slides and air-dried. Cells were fixed in 100% ice cold methanol for 3 minutes at -20°C. Afterwards, cells were blocked with 5% milk powder for 30 minutes. Next primary antibodies were diluted in PBS/3% milk powder and incubated for 2 hours, followed by three washing steps in PBS. Secondary antibodies were applied for 2 hours in PBS/3% milk powder containing 1 µg/ml Hoechst-33342 (Invitrogen) or DAPI (Roche) for nuclei staining, followed by 3 washes with PBS. One drop of mounting medium (Mowiol 4-88 (Calbiochem)) was added and the slide sealed with a coverslip for imaging.

To assess the localisation of the endogenously HA-tagged *Pf*PMRT1 IFAs were performed in suspension with Compound 2-stalled schizonts (86) to distinguish protein located at the PPM from that located at the PVM as previously done (51, 87). For this, trophozoite stages were treated with Compound 2 (1 µM) overnight, and arrested schizonts were harvested, washed in PBS, and fixed with 4% paraformaldehyde/0.0075% glutaraldehyde in PBS. Cells were permeabilized with 0.5% Triton X-100 in PBS, blocked with 3% BSA in PBS, and incubated overnight with primary antibodies diluted in 3% BSA in PBS. Cells were washed 3 times with PBS and incubated for 1 hour with Alexa 488 nm or Alexa 594 nm conjugated secondary antibodies specific for human and rat IgG (Invitrogen) diluted 1:2,000 in 3% BSA in PBS and containing 1 µg/ml DAPI. Cells were directly imaged after washing 5 times with PBS

Antisera used: 1:200 mouse anti-GFP clones 7.1 and 13.1 (Roche), 1:500 rat anti-HA clone 3F10 (Roche), 1:1000 human anti-MSP1 (88), 1:10000 mouse anti-TY1 (ThermoFischer Scientific Cat.No: MA5-23513). Contrast and intensities were linear adjusted if necessary and cropped images were assembled as panels using Fiji (89), Corel Photo-Paint X6 and Adobe Photoshop CC 2021.

**Immunoblots**

Immunoblots were performed using saponin lysed infected erythrocytes. Parasite proteins were separated on a 10% SDS-PAGE gel using standard procedures and transferred to a nitrocellulose membrane (Amersham™Protran™ 0.45 µm NC, GE Healthcare) using a transblot device (Bio-Rad) according to manufacturer's instructions.

Rabbit anti-aldolase (90) and anti-sbp1 (90) antibodies were diluted 1:2,000, mouse anti-GFP clones 7.1 and 13.1 (Roche) antibody was diluted 1:500 or 1:1,000 and rat anti-HA clone 3F10 (Roche) antibody was diluted 1:1,000.

The chemiluminescent signal of the HRP-coupled secondary antibodies (Dianova) was visualized using a Chemi Doc XRS imaging system (Bio-Rad) and processed with Image Lab Software 5.2 (Bio-Rad). To perform loading controls and ensure equal loading of parasite material anti-aldolase antibodies were used. The corresponding immunoblots were incubated two times in stripping buffer (0.2 M glycine, 50 mM DTT, 0.05% Tween 20) at 55°C for 1 hour and washed 3 times with TBS for 10 minutes.

**Growth Assay**

A flow cytometry-based assay adapted from previously published assays (40, 91) was performed. For this, parasite cultures were resuspended and 20 µl samples were transferred to an Eppendorf tube. 80 µl RPMI containing Hoechst-33342 and dihydroethidium (DHE) was added to obtain final concentrations of 5 µg/ml and 4.5 µg/ml, respectively. Samples were incubated for 20 minutes (protected from UV light) at room temperature, and parasitemia was determined using an LSRII flow cytometer by counting 100,000 events using the FACSDiva software (BD Biosciences) or using an ACEA NovoCyte flow cytometer.

**Stage distribution assay**

In order to obtain tightly synchronized parasite cultures, percoll purified schizonts(81) were cultured for four hours together with fresh erythrocytes, followed by sorbitol synchronization and resulting in a four-hour age window of parasites. Next, the culture was divided in four dishes and rapalog was added at a final concentration of 250 nM immediately to one dish and at 20 hours post invasion (hpi) and 32 hpi to the respective dishes. Giemsa smears and samples for flow cytometry were collected at the indicated timepoints. The parasitemia was determined using a flow cytometry assay and the stages were determined microscopically counting at least 50 infected erythrocytes per sample and timepoint.

**Gametocyte stage distribution assay**

Giemsa-stained blood smears 10 days post induction of GDV1 expression were obtained and at least 10 fields of view were recorded using a 63x objective per treatment and time point. Erythrocyte numbers were then determined using the automated Parasitemia software (http://www.gburri.org/parasitemia/) while the number of gametocytes, pycnotic and asexual parasites was determined manually in >1800 erythrocytes per sample. This assay was done blinded.

**GlmS-based knockdown**

GlmS based knockdown assay was adapted from previously published assays (38, 73). To induce knockdown 2.5 or 5 mM glucosamine was added to highly synchronous early rings stage parasites. As a control, the same amount of glucosamine was also added to 3D7 wildtype

552 parasites. For all analyses, the growth medium was changed daily, and fresh glucosamine
553 were added every day.
554 Knockdown was quantified by fluorescence live cell microscopy at day 1 and 3 of the growth
555 assay. Parasites with similar size were imaged, and fluorescence was captured with the same
556 acquisition settings to obtain comparable measurements of the fluorescence intensity.
557 Fluorescence intensity (integrated density) was measured with Fiji(89), and background was
558 subtracted in each image. The data were analyzed with Graph Pad Prism version 8.
559 GlmS based knockdown experiments in gametocytes were performed as described previously
560 (92). Briefly, synchronized ring stage cultures were induced by the addition of shield-1. At day
561 3 post induction the culture was spilt into two dishes and one dish was cultured in the presence
562 of 2.5 mM glucosamine for the remaining ten days. Knockdown was quantified by fluorescence
563 live cell microscopy at day 7 and 10 post induction, as described above and gametocyte
564 parasitemia was determined at day 10 post induction using the automated Parasitemia
565 software (http://www.gburri.org/parasitemia/).

566 **DiCre mediated conditional knockout**
567 The parasites containing the integrated pSLI-*Pf*PMRT1-loxP construct were transfected with
568 pSkip-Flox (37) using 2 µg/ml Blasticidin S to obtain a line expressing the DiCre fragments. To
569 induce excision, the tightly synchronized parasites (detailed description see growth assay)
570 were split into 2 dishes and rapalog was added to one dish (Clontech, Mountain View, CA) to
571 a final concentration of 250 nM. The untreated dish served as control culture. Excision was
572 verified at genomic level after 24 and 48 hours of cultivation by PCR and on protein level by
573 Western blot using anti-HA antibodies.

574 **Phylogenetic analysis**
575 A blastp search of the PMRT1 sequence (PlasmoDB (60): PF3D7_1135300; UniProt: Q8II12)
576 was performed against the nr database (9 May 2021) using Geneious Prime 2021.2.2
577 (https://www.geneious.com) and an E-value of 10e-0 (BLOSUM62 substitution matrix). Blast
578 hits were filtered for sequences from taxa represented in the currently favored haemosporidian
579 parasite phylogeny (93). The phylogeny derived from an amino acid alignment using Bayesian
580 framework with a partitioned supermatrix and a relaxed molecular clock
581 (18_amino_acid_partitioned_BEAST_relaxed_clock_no_outgroup.tre; (93)) was visualized
582 with associated data using the R package ggtree v3.3.0.900 (94, 95). A multiple protein
583 sequence alignment of PMRT1 and homologous sequences was performed using MAFFT
584 v7.490 (96) using the G-INS-I algorithm to obtain a highly accurate alignment. Protein statistics
585 were calculated using Geneious Prime 2021.2.2 (https://www.geneious.com) and EMBOSS
586 pepstats v6.6.0.0 (97).

587 **Prediction of protein structures**

AlphaFold structure predictions (35) were retrieved from https://alphafold.ebi.ac.uk and the PDB used for DALI protein structure homology search (36). PyMOL Molecular Graphics System, Version 2.5.2 Schrödinger was used for visualization of all structures, generation of figures and the calculation of the root mean square deviation (RMSD) between the predicted crystal structure of *Pf*PMRT1 and the Maquette-3 protein (PDB: 5vjt (57)) by cealign. The Adaptive Poisson-Boltzmann Solver (APBS) within PyMOL was used to predict the surface electrostatics of *Pf*PMRT1.

**Electrophysiology experiments**

Stage V and VI oocytes were surgically removed from female *Xenopus laevis* by immersion in water containing 1 g/L Tricain and isolated from theca and follicle layers by digestion with 0.14 mg $ml^{-1}$ collagenase I. Oocytes were injected with 20 ng cRNA and were incubated at 16ºC for 3 days in ND96 solution (96 mM NaCl, 2 mM KCl, 1 mM $CaCl_2$, 1 mM $MgCl_2$, 10 mM HEPES, pH7.4). Electrophysiological measurements with Xenopus oocytes were performed at room temperature (20–23ºC) with a two-electrode voltage clamp amplifier (TURBO TEC-03X, npi electronic GmbH, Tamm, Germany). The bath solutions for electrophysiological recording are indicated in each figure legend. Electrode capillaries (Φ=1.5 99 mm, Wall thickness 0.178 mm, Hilgenberg) were filled with 3 M KCl, with tip openings of 0.4–1 MΩ. USB-6221 DAQ device (National Instruments) and WinWCP (v5.5.3, Strathclyde University, UK) are used for data acquisition. Origin2020 Pro and the R software environment (98) were used for data analysis. Data was visualized in R using ggplot2 (99) and patchwork (100).

Parasite icons were generated using BioRender (biorender.com) and statistical analysis was performed using GraphPad Prism version 8 (GraphPad Software, USA).

**Acknowledgements**

We thank Michael Filarsky for providing the pHcamGDV1-GFP-DD_hDHFR plasmid, Egbert Tannich for providing *P. vivax* and *P. knowlesi* gDNA, Mike Blackman for the anti-MSP1 antibody, Jacobus Pharmaceuticals for WR99210, Greg Burri for the parasitemia software and the Advanced Light and Fluorescence Microscopy (ALFM) facility at the Centre for Structural Systems Biology (CSSB), in particular Roland Thuenauer, for support with light microscopy image recording and analysis. DSM1 (MRA-1161) was obtained from MR4/BEI Resources, NIAID, NIH. Furthermore, we thank Maria Rosenthal for her help with the visualization of the predicted protein structures.

**Funding**

AB and JSW were funded by the German Research Foundation (DFG) grant BA 5213/3-1. Partnership of Universität Hamburg and DESY (PIER) project ID PIF-2018-87 (JSTR, CL,

TWG), CSSB Seed grant KIF 2019/002 (TWG), Hospital Research Foundation Fellowship (DW), DAAD/Universities Australia joint research co-operation scheme (TWG, DW, BL). IH and BL were supported by Australian Government Research Training Stipend. JY, SG and GN were funded by DFG Projektnummer 374031971 TRR 240 A04 and 417451587. JSTÄ thanks the Jürgen Manchot Stiftung for funding and PMR, TS acknowledge funding by the DFG (SP1209/4-1)

**Author contribution**

Conceptualization: JSW, TWG, AB, JSTR

Methodology: GN, SG

Investigation: JSW, PMR, JY, GF; JSTÄ, HVT, AA, IH, BL

Formal Analysis: JSTR

Writing original manuscript: JSW, AB, JSTR, DW

Review & Editing: JSW, TWG, AB, JSTR, DW

Funding Acquisition: DW, CL, TWG, AB, JSTR

Resources: TWG

Project Administration: TWG, AB, JSTR

Supervision: DW, TS, SG, TWG, AB

All authors read and approved the manuscript.

**Figures**

**Figure 1: Subcellular localization of six putative *P. falciparum* transporters during asexual blood stage development.**

**(A)** Schematic representation of endogenous tagging strategy using the selection-linked integration system (SLI). pink, human dihydrofolate dehydrogenase (hDHFR); grey, homology region (HR); green, green fluorescence protein (GFP) tag; dark grey, T2A skip peptide; blue, neomycin resistance cassette; orange, glmS cassette. Stars indicate stop codons, and arrows depict primers (P1 to P4) used for the integration check PCR. **(B–G)** Localization of (B) *Pf*FVRT1-GFP-glmS, (C) *Pf*ZIP1-GFP-glmS, (D) *Pf*CDF-GFP-glmS, (E) *Pf*DMT2-GFP-glmS, (F) *Pf*MFS6-GFP-glmS and (G) *Pf*PMRT1-GFP-glmS by live-cell microscopy in ring, trophozoite and schizont stage parasites. Nuclei were stained with Hoechst-33342. **(H)** Co-localization of the GFP-tagged putative transporters with marker proteins P40PX-mCherry (food vacuole), ACP-mCherry (apicoplast), Lyn-mCherry (parasite plasma membrane), ARO-mCherry (rhoptry) and AMA1-mCherry (microneme) as indicated. Nuclei were stained with Hoechst- 33342. Scale bar, 2 µm.

**Figure 2: Conditional knockdown of putative transporter indicate importance of *Pf*DMT2 and *Pf*PMRT1 for parasites fitness.**

**(A–C)** Live cell microscopy and quantification of knockdown by measuring mean fluorescence intensity (MFI) density and size (area) of (A) *Pf*DMT2-GFP-glmS (B) *Pf*MFS6-GFP-glmS and (C) *Pf*PMRT1-GFP-glmS parasites 40 hours after treatment without (control) or with 2.5 mM glucosamine. Scale bar, 2 µm. Statistics are displayed as mean +/- SD of three (A–B) or four (C) independent experiments and individual data points are color-coded by experiments according to Superplots guidelines (101). P-values displayed were determined with two-tailed unpaired t-test. **(D)** Growth of parasites treated without (control) or with 2.5 mM glucosamine determined by flow cytometry is shown as relative parasitemia values after two cycles. Shown are means +/- SD of three (*Pf*PMRT1-GFP-glmS, *Pf*DMT2-GFP-glmS, *Pf*MFS6-GFP-glmS) and five (3D7 wild type parasites) independent growth experiments. P-values displayed were determined with unpaired t test with Welch correction and Benjamin Hochberg for multiple testing correction. Individual growth curves are shown in Figure S4G. **(E)** Growth of *Pf*PMRT1-glmS and 3D7 parasites after treatment with 2.5 mM (left panel) or 5 mM glucosamine (right panel) compared to untreated control parasites over five consecutive days. **(F)** Mean +/- SD distribution of ring and schizont stage parasites in *Pf*PMRT1-glmS and 3D7 cell lines treated without (control), with 2.5 mM or 5 mM glucosamine at 80 hours post addition of glucosamine of three independent experiments.

**Figure 3: *Pf*PMRT1 is essential for asexual blood stage development.**

**(A)** Simplified schematic of DiCre-based conditional *Pf*PMRT1 knockout using selection-linked integration (SLI). Pink, human dihydrofolate dehydrogenase (hDHFR); grey, homology region (HR); green, T2A skip peptide; light blue, recodonized *Pf*PMRT1; dark blue, 3xHA tag, yellow, neomycin phosphotransferase resistance cassette; orange, loxp sequence. Scissors indicate DiCre mediated excision sites upon addition of rapalog. Stars indicate stop codons, and arrows depict primers (P1 to P5) used for the integration check PCR and excision PCR. **(B)** Diagnostic PCR of unmodified wildtype and transgenic condΔPMRT1 knock-in (KI) cell line to check for genomic integration using Primer P1-P4 as indicated in (A). **(C)** Immunofluorescence assay (IFA) of condΔPMRT1 late stage schizont parasites showing localization of *Pf*PMRT1-3xHA at the parasite plasma membrane (PPM) co-localizing with the merozoite surface protein 1 (MSP1). **(D)** Diagnostic PCR to verify the excision at genomic level at 24 hpi / 20 hours post rapalog addition for condΔPMRT1 and at 48 hpi for condΔPMRT1, c-$^{nmd3}$*Pf*PMRT1-ty1 and c-$^{sf3a2}$*Pf*PMRT1-ty1 parasites using Primer P1-P5 as indicated in (A). Black arrow head, original locus; red arrow head, excised locus. **(E)** Western blot using α-HA to verify knockout of *Pf*PMRT1 on protein level 4, 24 and 48 hours post invasion. Expected molecular weight of *Pf*PMRT1-3xHA: 53.3 kDa. Antibodies detecting Aldolase and SBP1 were used as loading

controls. **(F)** Growth curves of condΔPMRT1, c-$^{nmd3}$*Pf*PMRT1-ty1 and c-$^{sf3a2}$*Pf*PMRT1-ty1 parasites +/- rapalog monitored over five days by flow cytometry. One representative growth curve is depicted (replicates in Figure S5). Summary is shown as relative parasitemia values, which were obtained by dividing the parasitemia of rapalog treated cultures by the parasitemia of the corresponding untreated ones. Shown are means +/- SD of three (condΔPMRT1, c-$^{nmd3}$*Pf*PMRT1-ty1) or four (c-$^{sf3a2}$*Pf*PMRT1-ty1) independent growth experiments. **(G)** IFA of condΔPMRT1 complemented with C-terminal TY1-tagged *Pf*PMRT1 constructs expressed either under the constitutive *nmd3* or the weak *sf3a2* promoter to verify PPM localization. Scale bar, 2 µm.

**Figure 4: Knockout of *Pf*PMRT1 results in accumulation of PPM-derived vacuoles and growth arrest at the trophozoite stage.**

**(A)** Parasite stage distribution in Giemsa smears displayed as heatmap showing percentage of parasite stages for tightly synchronized (+/- 2 h) 3D7 control and condΔPMRT1 (rapalog treated at 4 hpi, 20 hpi or 32 hpi) parasite cultures over two consecutive cycles. A second replicate is shown in Figure S6A **(B)** Giemsa smears of control and at 4 hpi rapalog treated condΔPMRT1 parasites over two cycles. Scale bar, 5 µm. **(C)** Live cell microscopy of 4 hour window synchronized 3D7 control and condΔPMRT1 parasites +/- rapalog stained with dihydroethidium (DHE) at 20–32 hpi. **(D)** Quantification of parasites displaying vacuoles (green) for 4 hour window synchronized 3D7 control and rapalog treated condΔPMRT1 parasites. Shown are percentages of normal parasites versus parasites displaying vacuoles as means +/- SD of three independent experiments. **(E)** Live cell microscopy of 8 hour window synchronized 3D7 control and rapalog treated condΔPMRT1 parasites, episomally expressing the PPM marker Lyn-mCherry at 24–40 hpi. **(F)** Live cell microscopy of 3D7 control and condΔPMRT1 parasites +/- rapalog stained with BODIPY TR C5 ceramide at 32 hpi. Scale bar, 2 µm.

**Figure 5: *Pf*PMRT1 is essential for early gametocyte development.**

**(A)** Live cell microscopy of 3D7-iGP-*Pf*PMRT1-GFP parasites across the complete gametocyte development. White arrow heads indicate remaining GDV1-GFP signal observed in close proximity to the Hoechst signal, as previously reported (56, 92, 102, 103). **(B)** Live cell microscopy of *Pf*PMRT1-GFP parasites expressing the PPM marker Lyn-mCherry. Nuclei were stained with Hoechst-33342. Scale bar, 2 µm. **(C)** Experimental setup of gametocyte induction upon GDV1-GFP-DD expression (+shield-1) and conditional *Pf*PMRT1 knockout (+rapalog) and elimination of asexual blood stage parasites (+GlcNac). **(D)** Gametocyte development over 12 days of condΔPMRT1/GDV1-GFP-DD parasites without (control) or with

rapalog addition at day 3 (3 dpi) or day 5 (5 dpi) after induction of sexual commitment by conditional expression of GDV1-GFP upon addition of shield-1. Scale bar, 5 µm. **(E)** Diagnostic PCR to verify the excision on genomic level at 5 dpi and 12 dpi. Black arrow head, original locus; red arrow head, excised locus. **(F)** Representative Giemsa smears and quantification of parasite stage distribution at day 10 post induction for parasites treated without (control) or with rapalog at day 3 post induction. For each condition parasitemia and parasite stages distribution in ($n_{control}$= 3370, 2304, 2759 and $n_{rapalog}$ = 3010, 1830, 2387) erythrocytes were determined and are displayed as percentage (gametocyte parasitemia for control (1.3%, 0.4%, 1.1%) and for rapalog treated (0%, 0%, 0%). Nuclei were stained with Hoechst-33342. Scale bar, 10 µm.

**Figure 6: PMRT1 is a genus-specific transporter with conserved function.**

**(A)** Phylogenetic tree of haemosporidian parasites (modified from (93)) containing PMRT1 homologous sequences associated with data on pairwise amino acid sequence identity to *Pf*PMRT1. The phylogeny is derived from Bayesian Inference using BEAST using a fully partitioned amino acid dataset and lognormal relaxed molecular clock (93). Silhouettes depict representatives of the vertebrate hosts for each lineage and white filled bars indicate pairwise identities of PMRT1 homologs used for subsequent complementation assays. **(B)** Structural alignment of predicted *Pf*PMRT1 structure with Maquette-3 protein (PDB: 5vjt) (57). Both structures have a root mean square deviation (RMSD) over the aligned α-carbon position of 3.12 over 184 residues calculated in PyMol. **(C)** IFA of c-$^{nmd3}$*Pk*-ty1 and c-$^{nmd3}$*Pv*-ty1 parasites to verify correct localization of the expressed complementation fusion proteins at the parasite plasma membrane. Nuclei were stained with Hoechst-33342. Scale bar, 2 µm. **(D)** Growth of condΔPMRT1 parasites complemented with *Pf*PMRT1 homologs from *P. vivax* (PVP01_0936100) and *P. knowlesi* (PKNH_0933400). Shown are relative parasitemia values, which were obtained by dividing the parasitemia of rapalog treated cultures by the parasitemia of the corresponding untreated controls together with means +/- SD from three c-$^{nmd3}$*Pf*-ty1 (≙ c-$^{nmd3}$*Pf*PMRT1-ty1 Figure 3D, S5B) and six (c-$^{nmd3}$*Pk*-ty1, c-$^{nmd3}$*Pv*-ty1) independent growth experiments. One sample t-test **(E)** Diagnostic PCR to verify the excision of *Pf*PMRT1 on genomic level at 48 hpi for c-$^{nmd3}$*Pf*-ty1, c-$^{nmd3}$*Pk*-ty1 and c-$^{nmd3}$*Pv*-ty1 parasites. Black arrow head, original locus; red arrow head, excised locus.

**Figure 7: *In vitro* characterization of *Pf*PMRT1 in *Xenopus* oocytes.**

**(A)** Surface electrostatics of the predicted *Pf*PMRT1 structure generated by APBS within PyMol. **(B)** Scheme of *Pf*PMRT1 membrane topology prediction and the two mutation sites: Outer loop mutant (MutPV) between TM 1 – 2 with negative charged amino acids (indicated in

red) and inner loop mutant (MutPC) between TM 4 – 5 with positive charged amino acids (indicated in blue) were changed to neutral amino acids. The cartoon was generated by Protter(104) and PyMol. **(C)** Confocal images of a non-injected oocyte, *Pf*PMRT1, MutPV and MutPC expressing oocytes. Scale bar, 100 µm. (**D)** Superimposed traces of control (injected with a cyclic nucleotide-gated potassium channel SthK(77)), *Pf*PMRT1, MutPV and MutPC expressing oocytes with the protocol shown in the upper left. The grey traces are original recordings from 7 to 10 oocytes, averaged traces are shown in black. Bath solution contains (in mM): 120 NMG Cl, 1 $MgCl_2$, 2 $CaCl_2$, 10 HEPES, pH7.6. **(E)** Current–voltage (I–V) curves of data points from (D) taken at the end of each holding potential. Both, MutPV and the SthK-control are significantly different from wild type *Pf*PMRT1 with P values of 0.017 and 0.014, respectively (Mean ± SD, n = 7 - 10). **(F)** Diagnostic PCR to verify the excision on genomic level at 48 hours post rapalog addition in cond∆PMRT1, c-$^{nmd3}$MutPC-ty1 and c-$^{nmd3}$MutPV-ty1 parasites +/- rapalog. Black arrow head, original locus; red arrow head, excised locus. **(G)** Parasite growth shown as relative parasitemia values, which were obtained by dividing the parasitemia of rapalog treated cultures by the parasitemia of the corresponding untreated controls. Shown are means +/- SD of four (c-$^{sf3a2}$ty1), three (c-$^{nmd3}$ty1, c-$^{nmd3}$MutPC-ty1), or six (c-$^{nmd}$-MutPV-ty1) independent growth experiments. One sample t-test was used to test for statistical differences between complemented cell lines and plus and minus rapalog treatment.

**Figure S1: Structure predictions and structure homology search of candidate proteins**
**(A)** AlphaFold structure predictions of the six selected orphan transporters visualized in PyMol. **(B)** Results from protein structure comparison server Dali using the AlphaFold-generated PDB files of the selected transporters as input structure. Shown are the top five non-redundant hits with Z score (significance estimate), msd (difference between the root-mean-square-deviation (rmsd) value associated with a protein structure pair and the rmsd value that would have been observed in the case that the two structures had the same crystallographic resolution), lali (number of aligned positions), nres (number of residues in the matched structure) and %id (the percentage sequence identity in the match).

**Figure S2: Validation of generated transgenic cell lines by PCR and Western blot.**
**(A)** Confirmatory PCR of unmodified wildtype (WT) and transgenic knock-in (KI) cell lines (PF3D7_0523800-GFP-glmS (*Pf*FVRT1), PF3D7_0609100-GFP-glmS (*Pf*ZIP1), PF3D7_0715900-GFP-glmS (*Pf*CDF), PF3D7_0716900-GFP-glmS (*Pf*DMT2), PF3D7_1440800-GFP-glmS (*Pf*MFS6) and PF3D7_1135300-GFP-glmS (*Pf*PMRT1)) to check for genomic integration at the 3'- and 5'-end of the locus. Position of the primer used are indicated with numbered arrows in Figure 1A. **(B)** Western Blot analysis of wildtype (3D7) and

804 knock-in (KI) cell lines using mouse anti-GFP to detect the tagged full-length protein (upper
805 panel) and rabbit anti-aldolase to control for equal loading (lower panel). Protein size is
806 indicated in kDa. Expected molecular weight for GFP fusion proteins: *Pf*FVRT1 (107.5 kDa),
807 *Pf*ZIP1 (69.0 kDa), *Pf*DMT2 (66.4 kDa), *Pf*MFS6 (98.8 kDa), *Pf*PMRT1 (77.5 kDa), *Pf*CDF
808 (91.6 kDa) **(C)** Localization of *Pf*CDF-3xHA by IFA in ring, trophozoite and schizont parasites.
809 Nuclei were stained with Hoechst. Diagnostic PCR of unmodified wildtype (WT) and transgenic
810 knock-in (KI) cell line. **(D)** Localization of *Pf*PMRT1_2xFKBP-GFP across the IDC. Nuclei were
811 stained with DAPI. Scale bar, 2 µm. Diagnostic PCR of unmodified wildtype (WT) and
812 transgenic knock-in (KI) cell line. (E) Localization of *Pf*ZIP1-GFP in merozoites. Nuclei were
813 stained with DAPI. Scale bar, 2 µm.
814

815 **Figure S3: Targeted gene disruption (TGD) of *Pf*ZIP1 and *Pf*CDF.**
816 **A)** Schematic representation of TGD strategy using the selection-linked integration system
817 (SLI). pink, human dihydrofolate dehydrogenase (hDHFR); grey, homology region (HR); green,
818 green fluorescence protein (GFP) tag; dark grey, T2A skip peptide; blue, neomycin resistance
819 cassette. Stars indicate stop codons, and arrows depict primers (P1 to P4) used for the
820 integration check PCR. **(B)** Localization of *Pf*ZIP1-TGD-GFP in ring, trophozoite and schizont
821 parasites. Nuclei were stained with Hoechst-33342. Scale bar, 2 µm. Confirmatory PCR of
822 unmodified wildtype (WT) and transgenic targeted gene disruption (TGD) cell line. Growth
823 curves of PfZIP1-TGD vs. 3D7 parasites monitored over five days by FACS. Three
824 independent growth experiments were performed and a summary is shown as percentage of
825 growth compared to 3D7 parasites. **(C)** Localization of *Pf*CDF-TGD in ring, trophozoite and
826 schizont parasites. Nuclei were stained with DAPI. Confirmatory PCR of unmodified wildtype
827 (WT) and transgenic targeted gene disruption (TGD) cell line. Scale bar, 1 µm.
828

829 **Figure S4: Conditional knockdown via glmS system.**
830 Live cell microscopy of **(A)** *Pf*FVRT1-GFP-glmS, **(B)** *Pf*CDF-GFP-glmS, **(C)** *Pf*ZIP1-GFP-glmS
831 **(D)** *Pf*DMT2-GFP-glmS, **(E)** *Pf*MFS6-GFP-glmS and **(F)** *Pf*PMRT1-GFP-glmS parasites 40
832 hours after treatment without (control) or with 2.5 mM Glucosamine. Nuclei were stained with
833 Hoechst-33342. Scale bar, 2 µm. **(G)** Individual growth curves of the growth assays shown in
834 Figure 2D.
835

836 **Figure S5: Conditional knockout of *Pf*PMRT1 via DiCre-based system**
837 Replicates of growth curves of condΔPMRT1, c-$^{nmd3}$*Pf*PMRT1-ty1 and c-$^{sf3a2}$*Pf*PMRT1-ty1
838 parasites +/- rapalog monitored over five days by FACS shown in Figure 3.
839

**Figure S6: Conditional knockout of *Pf*PMRT1**

**(A)** Parasite stage distribution in Giemsa smears displayed as heatmap showing percentage of stages for control, 4 hpi, 20 hpi or 32 hpi rapalog treated 4 hour window synchronized condΔPMRT1parasite cultures over one cycle. **(B)** Giemsa smears of control and 4 hpi, 20 hpi or 32 hpi rapalog treated parasites at 4, 16, 20, 24, 32, 40 and 48 hpi. Scale bar, 5 µm.

**Figure S7: Conditional knockdown of *Pf*PMRT1 has no effect during gametocyte development.**

**(A)** Confirmatory PCR of unmodified wildtype (WT) and transgenic 3D7-iGP-*Pf*PMRT1-GFP-glmS to check for genomic integration at the 3'- and 5'-end of the locus. Position of the primer used are indicated with numbered arrows in Figure 1A. **(B)** Schematic representation of the experimental setup. **(C)** Live cell microscopy of 3D7-iGP-*Pf*PMRT1-GFP stage I – V gametocytes. Scale bar, 2 µm. **(D)** Giemsa smears of stage I – V gametocytes cultured either without (control) or with 2.5 mM glucosamine. Scale bar, 5 µm. **(E)** Quantification of knockdown by measuring mean fluorescence intensity (MFI) density and size (area) of parasites at day 7 and day 12 post induction of gametocytogenesis cultured either without (control) or with 2.5 mM glucosamine. Scale bar, 2 µm. Statistics are displayed as mean +/- SD of four independent experiments and individual data points are displayed as scatterplot color-coded by experiments according to Superplots guidelines(101)(101). P-values displayed were determined with two-tailed unpaired t-test. **(F)** For each condition gametocytemia at day 10 post gametocyte induction was determined by counting between 1256-2653 (mean 2147) cells per condition in Giemsa-stained thin blood smears. Displayed are means +/- SD of independent growth experiments with the number of experiments (n) indicated. P-values displayed were determined with two-tailed unpaired t-test.

**Figure S8:** Individual growth curves of c-$^{nmd3}$*Pk*-ty1 (A) and c-$^{nmd3}$*Pv*-ty1 (B) parasites +/- rapalog monitored over two IDCs by FACS shown in Figure 6.

**Figure S9:** Individual growth curves of c-$^{nmd3}$MutIn-ty1 (A) and c-$^{nmd3}$MutOut-ty1 (B) parasites +/- rapalog monitored over two IDCs by FACS shown in Figure 7. **(C)** IFA of c-$^{nmd3}$MutPC-ty1 and c-$^{nmd3}$MutPV-ty1 parasites to verify correct localization at the parasite plasma membrane. Nuclei were stained with Hoechst-33342. Scale bar, 2 µm.

**Table S1: Oligonucleotides and plasmids used in this study**

## References

1. Martin RE, Henry RI, Abbey JL, Clements JD, Kirk K. 2005. The “permeome” of the malaria parasite: an overview of the membrane transport proteins of Plasmodium falciparum. Genome Biol 6:R26.
2. Martin RE. 2020. The transportome of the malaria parasite. Biol Rev Camb Philos Soc 95:305–332.
3. Gardner MJ, Hall N, Fung E, White O, Berriman M, Hyman RW, Carlton JM, Pain A, Nelson KE, Bowman S, Paulsen IT, James K, Eisen JA, Rutherford K, Salzberg SL, Craig A, Kyes S, Chan M-S, Nene V, Shallom SJ, Suh B, Peterson J, Angiuoli S, Pertea M, Allen J, Selengut J, Haft D, Mather MW, Vaidya AB, Martin DMA, Fairlamb AH, Fraunholz MJ, Roos DS, Ralph SA, McFadden GI, Cummings LM, Subramanian GM, Mungall C, Venter JC, Carucci DJ, Hoffman SL, Newbold C, Davis RW, Fraser CM, Barrell B. 2002. Genome sequence of the human malaria parasite Plasmodium falciparum. Nature 419:498–511.
4. Martin RE, Ginsburg H, Kirk K. 2009. Membrane transport proteins of the malaria parasite. Mol Microbiol. John Wiley & Sons, Ltd (10.1111).
5. Weiner J, Kooij TWA. 2016. Phylogenetic profiles of all membrane transport proteins of the malaria parasite highlight new drug targets. Microb Cell 3:511–521.
6. Dean P, Major P, Nakjang S, Hirt RP, Martin Embley T. 2014. Transport proteins of parasitic protists and their role in nutrient salvage. Front Plant Sci. Frontiers Research Foundation.
7. Foote SJ, Thompson JK, Cowman AF, Kemp DJ. 1989. Amplification of the multidrug resistance gene in some chloroquine-resistant isolates of P. falciparum. Cell 57:921–930.
8. Fidock DA, Nomura T, Talley AK, Cooper RA, Dzekunov SM, Ferdig MT, Ursos LMB, Bir Singh Sidhu A, Naudé B, Deitsch KW, Su XZ, Wootton JC, Roepe PD, Wellems TE. 2000. Mutations in the P. falciparum digestive vacuole transmembrane protein PfCRT and evidence for their role in chloroquine resistance. Mol Cell 6:861–871.
9. Veiga MI, Dhingra SK, Henrich PP, Straimer J, Gnädig N, Uhlemann AC, Martin RE, Lehane AM, Fidock DA. 2016. Globally prevalent PfMDR1 mutations modulate Plasmodium falciparum susceptibility to artemisinin-based combination therapies. Nat Commun 7.
10. Rijpma SR, Van Der Velden M, Bilos A, Jansen RS, Mahakena S, Russel FGM, Sauerwein RW, Van De Wetering K, Koenderink JB. 2016. MRP1 mediates folate transport and antifolate sensitivity in Plasmodium falciparum. FEBS Lett 590:482–492.
11. Mesén-Ramírez P, Bergmann B, Elhabiri M, Zhu L, Thien H von, Castro-Peña C, Gilberger T-W, Davioud-Charvet E, Bozdech Z, Bachmann A, Spielmann T. 2021. The

parasitophorous vacuole nutrient pore is critical for drug access in malaria parasites and modulates the fitness cost of artemisinin resistance. Cell Host Microbe 0:283.

12. Cowman AF, Galatis D, Thompson JK. 1994. Selection for mefloquine resistance in Plasmodium falciparum is linked to amplification of the pfmdr1 gene and cross-resistance to halofantrine and quinine. Proc Natl Acad Sci U S A 91:1143–1147.

13. Mok S, Liong KY, Lim EH, Huang X, Zhu L, Preiser PR, Bozdech Z. 2014. Structural polymorphism in the promoter of pfmrp2 confers Plasmodium falciparum tolerance to quinoline drugs. Mol Microbiol 91:918–934.

14. Lim MYX, LaMonte G, Lee MCS, Reimer C, Tan BH, Corey V, Tjahjadi BF, Chua A, Nachon M, Wintjens R, Gedeck P, Malleret B, Renia L, Bonamy GMC, Ho PCL, Yeung BKS, Chow ED, Lim L, Fidock DA, Diagana TT, Winzeler EA, Bifani P. 2016. UDP-galactose and acetyl-CoA transporters as Plasmodium multidrug resistance genes. Nat Microbiol 1.

15. Richards SN, Nash MN, Baker ES, Webster MW, Lehane AM, Shafik SH, Martin RE. 2016. Molecular Mechanisms for Drug Hypersensitivity Induced by the Malaria Parasite's Chloroquine Resistance Transporter. PLoS Pathog 12.

16. Cowell AN, Istvan ES, Lukens AK, Gomez-Lorenzo MG, Vanaerschot M, Sakata-Kato T, Flannery EL, Magistrado P, Owen E, Abraham M, La Monte G, Painter HJ, Williams RM, Franco V, Linares M, Arriaga I, Bopp S, Corey VC, Gnädig NF, Coburn-Flynn O, Reimer C, Gupta P, Murithi JM, Moura PA, Fuchs O, Sasaki E, Kim SW, Teng CH, Wang LT, Akidil A, Adjalley S, Willis PA, Siegel D, Tanaseichuk O, Zhong Y, Zhou Y, Llinás M, Ottilie S, Gamo FJ, Lee MCS, Goldberg DE, Fidock DA, Wirth DF, Winzeler EA. 2018. Mapping the malaria parasite druggable genome by using in vitro evolution and chemogenomics. Science (80- ) 359:191–199.

17. Rocamora F, Gupta P, Istvan ES, Luth MR, Carpenter EF, Kümpornsin K, Sasaki E, Calla J, Mittal N, Carolino K, Owen E, Llinás M, Ottilie S, Goldberg DE, Lee MCS, Winzeler EA. 2021. PfMFR3: A Multidrug-Resistant Modulator in Plasmodium falciparum. ACS Infect Dis 7:811–825.

18. Kirk K. 2004. Channels and transporters as drug targets in the Plasmodium-infected erythrocyte. Acta Trop 89:285–298.

19. Koenderink JB, Kavishe RA, Rijpma SR, Russel FGM. 2010. The ABCs of multidrug resistance in malaria. Trends Parasitol. Trends Parasitol.

20. Murithi JM, Deni I, Pasaje CFA, Okombo J, Bridgford JL, Gnädig NF, Edwards RL, Yeo T, Mok S, Burkhard AY, Coburn-Flynn O, Istvan ES, Sakata-Kato T, Gomez-Lorenzo MG, Cowell AN, Wicht KJ, Le Manach C, Kalantarov GF, Dey S, Duffey M, Laleu B, Lukens AK, Ottilie S, Vanaerschot M, Trakht IN, Gamo F-J, Wirth DF, Goldberg DE, Odom John AR, Chibale K, Winzeler EA, Niles JC, Fidock DA. 2021. The Plasmodium

falciparum ABC transporter ABCI3 confers parasite strain-dependent pleiotropic antimalarial drug resistance. Cell Chem Biol 0.

21. Counihan NA, Modak JK, de Koning-Ward TF. 2021. How Malaria Parasites Acquire Nutrients From Their Host. Front Cell Dev Biol 9:582.

22. Saliba KJ, Horner HA, Kirk K. 1998. Transport and metabolism of the essential vitamin pantothenic acid in human erythrocytes infected with the malaria parasite Plasmodium falciparum. J Biol Chem 273:10190–10195.

23. Gulati S, Ekland EH, Ruggles K V., Chan RB, Jayabalasingham B, Zhou B, Mantel PY, Lee MCS, Spottiswoode N, Coburn-Flynn O, Hjelmqvist D, Worgall TS, Marti M, Di Paolo G, Fidock DA. 2015. Profiling the Essential Nature of Lipid Metabolism in Asexual Blood and Gametocyte Stages of Plasmodium falciparum. Cell Host Microbe 18:371–381.

24. Mamoun C Ben, Prigge ST, Vial H. 2010. Targeting the lipid metabolic pathways for the treatment of malaria. Drug Dev Res. John Wiley & Sons, Ltd.

25. Garten M, Beck JR. 2021. Structured to conquer: transport across the Plasmodium parasitophorous vacuole. Curr Opin Microbiol. Elsevier Ltd.

26. Kloehn J, Lacour CE, Soldati-Favre D. 2021. The metabolic pathways and transporters of the plastid organelle in Apicomplexa. Curr Opin Microbiol 63:250–258.

27. Beck JR, Ho CM. 2021. Transport mechanisms at the malaria parasite-host cell interface. PLoS Pathog. Public Library of Science.

28. Kenthirapalan S, Waters AP, Matuschewski K, Kooij TWA. 2016. Functional profiles of orphan membrane transporters in the life cycle of the malaria parasite. Nat Commun 7:10519.

29. Sayers CP, Mollard V, Buchanan HD, McFadden GI, Goodman CD. 2018. A genetic screen in rodent malaria parasites identifies five new apicoplast putative membrane transporters, one of which is essential in human malaria parasites. Cell Microbiol 20:e12789.

30. Ginsburg H. 2006. Progress in in silico functional genomics: the malaria Metabolic Pathways database. Trends Parasitol 22:238–240.

31. Otto TD, Wilinski D, Assefa S, Keane TM, Sarry LR, Böhme U, Lemieux J, Barrell B, Pain A, Berriman M, Newbold C, Llinás M. 2010. New insights into the blood-stage transcriptome of Plasmodium falciparum using RNA-Seq. Mol Microbiol 76:12–24.

32. Wichers JS, Scholz JAM, Strauss J, Witt S, Lill A, Ehnold LI, Neupert N, Liffner B, Lühken R, Petter M, Lorenzen S, Wilson DW, Löw C, Lavazec C, Bruchhaus I, Tannich E, Gilberger TW, Bachmann A. 2019. Dissecting the gene expression, localization, membrane topology, and function of the plasmodium falciparum STEVOR protein family. MBio 10:e01500-19.

986 33. Treeck M, Sanders JL, Elias JE, Boothroyd JC. 2011. The phosphoproteomes of
987 plasmodium falciparum and toxoplasma gondii reveal unusual adaptations within and
988 beyond the parasites' boundaries. Cell Host Microbe 10:410–419.
989 34. Pease BN, Huttlin EL, Jedrychowski MP, Talevich E, Harmon J, Dillman T, Kannan N,
990 Doerig C, Chakrabarti R, Gygi SP, Chakrabarti D. 2013. Global analysis of protein
991 expression and phosphorylation of three stages of plasmodium falciparum
992 intraerythrocytic development. J Proteome Res 12:4028–4045.
993 35. Jumper J, Evans R, Pritzel A, Green T, Figurnov M, Ronneberger O, Tunyasuvunakool
994 K, Bates R, Žídek A, Potapenko A, Bridgland A, Meyer C, Kohl SAA, Ballard AJ, Cowie
995 A, Romera-Paredes B, Nikolov S, Jain R, Adler J, Back T, Petersen S, Reiman D,
996 Clancy E, Zielinski M, Steinegger M, Pacholska M, Berghammer T, Bodenstein S, Silver
997 D, Vinyals O, Senior AW, Kavukcuoglu K, Kohli P, Hassabis D. 2021. Highly accurate
998 protein structure prediction with AlphaFold. Nature 596:583–589.
999 36. Holm L. 2020. DALI and the persistence of protein shape. Protein Sci 29:128–140.
1000 37. Birnbaum J, Flemming S, Reichard N, Soares AB, Mesén-Ramírez P, Jonscher E,
1001 Bergmann B, Spielmann T. 2017. A genetic system to study Plasmodium falciparum
1002 protein function. Nat Methods 14:450–456.
1003 38. Prommana P, Uthaipibull C, Wongsombat C, Kamchonwongpaisan S, Yuthavong Y,
1004 Knuepfer E, Holder AA, Shaw PJ. 2013. Inducible Knockdown of Plasmodium Gene
1005 Expression Using the glmS Ribozyme. PLoS One 8:e73783.
1006 39. Tawk L, Chicanne G, Dubremetz J-F, Richard V, Payrastre B, Vial HJ, Roy C, Wengelnik
1007 K. 2010. Phosphatidylinositol 3-Phosphate, an Essential Lipid in Plasmodium, Localizes
1008 to the Food Vacuole Membrane and the Apicoplast. Eukaryot Cell 9:1519–1530.
1009 40. Jonscher E, Flemming S, Schmitt M, Sabitzki R, Reichard N, Birnbaum J, Bergmann B,
1010 Höhn K, Spielmann T. 2019. PfVPS45 Is Required for Host Cell Cytosol Uptake by
1011 Malaria Blood Stage Parasites. Cell Host Microbe 25:166-173.e5.
1012 41. Waller RF, Reed MB, Cowman AF, McFadden GI. 2000. Protein trafficking to the plastid
1013 of Plasmodium falciparum is via the secretory pathway. EMBO J 19:1794–1802.
1014 42. Birnbaum J, Scharf S, Schmidt S, Jonscher E, Hoeijmakers WAM, Flemming S,
1015 Toenhake CG, Schmitt M, Sabitzki R, Bergmann B, Fröhlke U, Mesén-Ramírez P,
1016 Blancke Soares A, Herrmann H, Bártfai R, Spielmann T. 2020. A Kelch13-defined
1017 endocytosis pathway mediates artemisinin resistance in malaria parasites. Science (80-
1018 ) 367:51–59.
1019 43. Inoue T, Heo W Do, Grimley JS, Wandless TJ, Meyer T. 2005. An inducible translocation
1020 strategy to rapidly activate and inhibit small GTPase signaling pathways. Nat Methods
1021 2:415–418.
1022 44. Cabrera A, Herrmann S, Warszta D, Santos JM, John Peter AT, Kono M, Debrouver S,

Jacobs T, Spielmann T, Ungermann C, Soldati-Favre D, Gilberger TW. 2012. Dissection of Minimal Sequence Requirements for Rhoptry Membrane Targeting in the Malaria Parasite. Traffic 13:1335–1350.

45. Geiger M, Brown C, Wichers JS, Strauss J, Lill A, Thuenauer R, Liffner B, Wilcke L, Lemcke S, Heincke D, Pazicky S, Bachmann A, Löw C, Wilson DW, Filarsky M, Burda P-C, Zhang K, Junop M, Gilberger TW. 2020. Structural Insights Into PfARO and Characterization of its Interaction With PfAIP. J Mol Biol 432:878–896.

46. Peterson MG, Marshall VM, Smythe JA, Crewther PE, Lew A, Silva A, Anders RF, Kemp DJ. 1989. Integral membrane protein located in the apical complex of Plasmodium falciparum. Mol Cell Biol 9:3151–3154.

47. Wichers JS, Wunderlich J, Heincke D, Pazicky S, Strauss J, Schmitt M, Kimmel J, Wilcke L, Scharf S, von Thien H, Burda P, Spielmann T, Löw C, Filarsky M, Bachmann A, Gilberger TW. 2021. Identification of novel inner membrane complex and apical annuli proteins of the malaria parasite Plasmodium falciparum. Cell Microbiol 23:e13341.

48. Jullien N, Goddard I, Selmi-Ruby S, Fina J-L, Cremer H, Herman J-P. 2007. Conditional Transgenesis Using Dimerizable Cre (DiCre). PLoS One 2:e1355.

49. Andenmatten N, Egarter S, Jackson AJ, Jullien N, Herman JP, Meissner M. 2013. Conditional genome engineering in Toxoplasma gondii uncovers alternative invasion mechanisms. Nat Methods 10:125–127.

50. Holder AA, Lockyer MJ, Odink KG, Sandhu JS, Riveros-Moreno V, Nicholls SC, Hillman Y, Davey LS, Tizard MLV, Schwarz RT, Freeman RR. 1985. Primary structure of the precursor to the three major surface antigens of Plasmodium falciparum merozoites. Nature 317:270–273.

51. Mesén-Ramírez P, Bergmann B, Tran TT, Garten M, Stäcker J, Naranjo-Prado I, Höhn K, Zimmerberg J, Spielmann T. 2019. EXP1 is critical for nutrient uptake across the parasitophorous vacuole membrane of malaria parasites. PLoS Biol 17:e3000473.

52. López-Barragán MJ, Lemieux J, Quiñones M, Williamson KC, Molina-Cruz A, Cui K, Barillas-Mury C, Zhao K, Su X zhuan. 2011. Directional gene expression and antisense transcripts in sexual and asexual stages of Plasmodium falciparum. BMC Genomics 12:587.

53. Lasonder E, Rijpma SR, Van Schaijk BCL, Hoeijmakers WAM, Kensche PR, Gresnigt MS, Italiaander A, Vos MW, Woestenenk R, Bousema T, Mair GR, Khan SM, Janse CJ, Bártfai R, Sauerwein RW. 2016. Integrated transcriptomic and proteomic analyses of P. Falciparum gametocytes: Molecular insight into sex-specific processes and translational repression. Nucleic Acids Res 44:6087–6101.

54. Gómez-Díaz E, Yerbanga RS, Lefèvre T, Cohuet A, Rowley MJ, Ouedraogo JB, Corces

VG. 2017. Epigenetic regulation of Plasmodium falciparum clonally variant gene expression during development in Anopheles gambiae. Sci Rep 7.

55. Boltryk SD, Passecker A, Alder A, Carrington E, van de Vegte-Bolmer M, van Gemert G-J, van der Starre A, Beck H-P, Sauerwein RW, Kooij TWA, Brancucci NMB, Proellochs NI, Gilberger T-W, Voss TS. 2021. CRISPR/Cas9-engineered inducible gametocyte producer lines as a valuable tool for Plasmodium falciparum malaria transmission research. Nat Commun 12:4806.

56. Filarsky M, Fraschka SA, Niederwieser I, Brancucci NMB, Carrington E, Carrió E, Moes S, Jenoe P, Bártfai R, Voss TS. 2018. GDV1 induces sexual commitment of malaria parasites by antagonizing HP1-dependent gene silencing. Science (80- ) 359:1259–1263.

57. Ennist NM, Stayrook SE, Dutton PL, Moser CC. 2017. 5VJT: De Novo Photosynthetic Reaction Center Protein Equipped with Heme B and Zn(II) cations. doi: 10.2210/pdb5vjt/pdb

58. Sonnhammer EL, von Heijne G, Krogh A. 1998. A hidden Markov model for predicting transmembrane helices in protein sequences. Proceedings Int Conf Intell Syst Mol Biol 6:175–82.

59. Käll L, Krogh A, Sonnhammer ELL. 2004. A combined transmembrane topology and signal peptide prediction method. J Mol Biol 338:1027–1036.

60. Aurrecoechea C, Brestelli J, Brunk BP, Dommer J, Fischer S, Gajria B, Gao X, Gingle A, Grant G, Harb OS, Heiges M, Innamorato F, Iodice J, Kissinger JC, Kraemer E, Li W, Miller JA, Nayak V, Pennington C, Pinney DF, Roos DS, Ross C, Stoeckert CJ, Treatman C, Wang H. 2009. PlasmoDB: a functional genomic database for malaria parasites. Nucleic Acids Res 37:D539–D543.

61. Wunderlich J, Rohrbach P, Dalton JP. 2012. The malaria digestive vacuole. Front Biosci (Schol Ed) 4:1424–48.

62. Tabuchi M, Yoshimori T, Yamaguchi K, Yoshida T, Kishi F. 2000. Human NRAMP2/DMT1, which mediates iron transport across endosomal membranes, is localized to late endosomes and lysosomes in HEp-2 cells. J Biol Chem 275:22220–22228.

63. Zhang M, Wang C, Otto TD, Oberstaller J, Liao X, Adapa SR, Udenze K, Bronner IF, Casandra D, Mayho M, Brown J, Li S, Swanson J, Rayner JC, Jiang RHY, Adams JH. 2018. Uncovering the essential genes of the human malaria parasite Plasmodium falciparum by saturation mutagenesis. Science 360:eaap7847.

64. Kennedy K, Cobbold SA, Hanssen E, Birnbaum J, Spillman NJ, McHugh E, Brown H, Tilley L, Spielmann T, McConville MJ, Ralph SA. 2019. Delayed death in the malaria parasite Plasmodium falciparum is caused by disruption of prenylation-dependent

intracellular trafficking. PLOS Biol 17:e3000376.

65. Pasaje CFA, Cheung V, Kennedy K, Lim EE, Baell JB, Griffin MDW, Ralph SA. 2016. Selective inhibition of apicoplast tryptophanyl-tRNA synthetase causes delayed death in Plasmodium falciparum. Sci Rep 6:1–13.

66. Yeh E, DeRisi JL. 2011. Chemical rescue of malaria parasites lacking an apicoplast defines organelle function in blood-stage plasmodium falciparum. PLoS Biol 9.

67. Bushell E, Gomes AR, Sanderson T, Anar B, Girling G, Herd C, Metcalf T, Modrzynska K, Schwach F, Martin RE, Mather MW, McFadden GI, Parts L, Rutledge GG, Vaidya AB, Wengelnik K, Rayner JC, Billker O. 2017. Functional Profiling of a Plasmodium Genome Reveals an Abundance of Essential Genes. Cell 170:260-272.e8.

68. Chasen NM, Stasic AJ, Asady B, Coppens I, Moreno SNJ. 2019. The Vacuolar Zinc Transporter TgZnT Protects Toxoplasma gondii from Zinc Toxicity. mSphere 4:e00086-19.

69. Jiang Y, Wei J, Cui H, Liu C, Zhi Y, Jiang Z, Li Z, Li S, Yang Z, Wang X, Qian P, Zhang C, Zhong C, Su X, Yuan J. 2020. An intracellular membrane protein GEP1 regulates xanthurenic acid induced gametogenesis of malaria parasites. Nat Commun 11:1764.

70. Liu W, Sundararaman SA, Loy DE, Learn GH, Li Y, Plenderleith LJ, Ndjango JBN, Speede S, Atencia R, Cox D, Shaw GM, Ayouba A, Peeters M, Rayner JC, Hahn BH, Sharp PM. 2016. Multigenomic delineation of Plasmodium species of the Laverania subgenus infecting wild-living chimpanzees and gorillas. Genome Biol Evol 8:1929–1939.

71. Zanghì G, Vembar SS, Baumgarten S, Ding S, Guizetti J, Bryant JM, Mattei D, Jensen ATR, Rénia L, Goh YS, Sauerwein R, Hermsen CC, Franetich J-F, Bordessoulles M, Silvie O, Soulard V, Scatton O, Chen P, Mecheri S, Mazier D, Scherf A. 2018. A Specific PfEMP1 Is Expressed in P. falciparum Sporozoites and Plays a Role in Hepatocyte Infection. Cell Rep 22:2951–2963.

72. Howick VM, Russell AJC, Andrews T, Heaton H, Reid AJ, Natarajan K, Butungi H, Metcalf T, Verzier LH, Rayner JC, Berriman M, Herren JK, Billker O, Hemberg M, Talman AM, Lawniczak MKN. 2019. The malaria cell atlas: Single parasite transcriptomes across the complete Plasmodium life cycle. Science (80- ) 365.

73. Burda P-C, Crosskey T, Lauk K, Zurborg A, Söhnchen C, Liffner B, Wilcke L, Strauss J, Jeffries CM, Svergun DI, Wilson DW, Wilmanns M, Gilberger T-W, Pietsch E, Strauss J, Jeffries CM, Svergun DI, Wilson DW, Wilmanns M, Gilberger T-W. 2020. Structure-Based Identification and Functional Characterization of a Lipocalin in the Malaria Parasite Plasmodium falciparum. Cell Rep 31:107817.

74. Auburn S, Böhme U, Steinbiss S, Trimarsanto H, Hostetler J, Sanders M, Gao Q, Nosten F, Newbold CI, Berriman M, Price RN, Otto TD. 2016. A new Plasmodium vivax

reference sequence with improved assembly of the subtelomeres reveals an abundance of pir genes. Wellcome Open Res 1:4.

75. Pain A, Böhme U, Berry AE, Mungall K, Finn RD, Jackson AP, Mourier T, Mistry J, Pasini EM, Aslett MA, Balasubrammaniam S, Borgwardt K, Brooks K, Carret C, Carver TJ, Cherevach I, Chillingworth T, Clark TG, Galinski MR, Hall N, Harper D, Harris D, Hauser H, Ivens A, Janssen CS, Keane T, Larke N, Lapp S, Marti M, Moule S, Meyer IM, Ormond D, Peters N, Sanders M, Sanders S, Sargeant TJ, Simmonds M, Smith F, Squares R, Thurston S, Tivey AR, Walker D, White B, Zuiderwijk E, Churcher C, Quail MA, Cowman AF, Turner CMR, Rajandream MA, Kocken CHM, Thomas AW, Newbold CI, Barrell BG, Berriman M. 2008. The genome of the simian and human malaria parasite Plasmodium knowlesi. Nature 455:799–803.

76. Liman ER, Tytgat J, Hess P. 1992. Subunit stoichiometry of a mammalian K+ channel determined by construction of multimeric cDNAs. Neuron 9:861–871.

77. Beck S, Yu-Strzelczyk J, Pauls D, Constantin OM, Gee CE, Ehmann N, Kittel RJ, Nagel G, Gao S. 2018. Synthetic Light-Activated Ion Channels for Optogenetic Activation and Inhibition. Front Neurosci 12:643.

78. Trager W, Jensen JB. 1997. Continuous culture of Plasmodium falciparum: its impact on malaria research. Int J Parasitol 27:989–1006.

79. Lambros C, Vanderberg JP. 1979. Synchronization of Plasmodium falciparum Erythrocytic Stages in Culture. J Parasitol 65:418.

80. Ponnudurai T, Lensen AHW, Meis JFGM, Meuwissen JHE. 1986. Synchronization of Plasmodium falciparum gametocytes using an automated suspension culture system. Parasitology 93:263–274.

81. Rivadeneira E, Wasserman M, Espinal C. 1983. Separation and Concentration of Schizonts of Plasmodium falciparum by Percoll Gradients. J Protozool 30:367–370.

82. Moon RW, Hall J, Rangkuti F, Ho YS, Almond N, Mitchell GH, Pain A, Holder AA, Blackman MJ. 2013. Adaptation of the genetically tractable malaria pathogen Plasmodium knowlesi to continuous culture in human erythrocytes. Proc Natl Acad Sci 110:531–536.

83. Ganesan SM, Morrisey JM, Ke H, Painter HJ, Laroiya K, Phillips MA, Rathod PK, Mather MW, Vaidya AB. 2011. Yeast dihydroorotate dehydrogenase as a new selectable marker for Plasmodium falciparum transfection. Mol Biochem Parasitol 177:29–34.

84. Grüring C, Spielmann T. 2012. Imaging of live malaria blood stage parasites. Methods Enzymol 506:81–92.

85. Bachmann A, Scholz JAM, Janßen M, Klinkert M-Q, Tannich E, Bruchhaus I, Petter M. 2015. A comparative study of the localization and membrane topology of members of the RIFIN, STEVOR and PfMC-2TM protein families in Plasmodium falciparum-infected

erythrocytes. Malar J 14:274.

86. Collins CR, Hackett F, Strath M, Penzo M, Withers-Martinez C, Baker DA, Blackman MJ. 2013. Malaria Parasite cGMP-dependent Protein Kinase Regulates Blood Stage Merozoite Secretory Organelle Discharge and Egress. PLoS Pathog 9:e1003344.

87. Tonkin CJ, Van Dooren GG, Spurck TP, Struck NS, Good RT, Handman E, Cowman AF, McFadden GI. 2004. Localization of organellar proteins in Plasmodium falciparum using a novel set of transfection vectors and a new immunofluorescence fixation method. Mol Biochem Parasitol 137:13–21.

88. Blackman MJ, Whittle H, Holder AA. 1991. Processing of the Plasmodium falciparum major merozoite surface protein-1: identification of a 33-kilodalton secondary processing product which is shed prior to erythrocyte invasion. Mol Biochem Parasitol 49:35–44.

89. Schindelin J, Arganda-Carreras I, Frise E, Kaynig V, Longair M, Pietzsch T, Preibisch S, Rueden C, Saalfeld S, Schmid B, Tinevez J-Y, White DJ, Hartenstein V, Eliceiri K, Tomancak P, Cardona A. 2012. Fiji: an open-source platform for biological-image analysis. Nat Methods 9:676–682.

90. Mesén-Ramírez P, Reinsch F, Blancke Soares A, Bergmann B, Ullrich AK, Tenzer S, Spielmann T. 2016. Stable Translocation Intermediates Jam Global Protein Export in Plasmodium falciparum Parasites and Link the PTEX Component EXP2 with Translocation Activity. PLoS Pathog 12:e1005618.

91. Malleret B, Claser C, Ong ASM, Suwanarusk R, Sriprawat K, Howland SW, Russell B, Nosten F, Rénia L. 2011. A rapid and robust tri-color flow cytometry assay for monitoring malaria parasite development. Sci Rep 1:118.

92. Wichers JS, van Gelder C, Fuchs G, Ruge JM, Pietsch E, Ferreira JL, Safavi S, von Thien H, Burda P-C, Mesén-Ramirez P, Spielmann T, Strauss J, Gilberger T-W, Bachmann A. 2021. Characterization of Apicomplexan Amino Acid Transporters (ApiATs) in the Malaria Parasite Plasmodium falciparum. mSphere https://doi.org/10.1128/mSphere.00743-21.

93. Galen SC, Borner J, Martinsen ES, Schaer J, Austin CC, West CJ, Perkins SL. 2018. The polyphyly of Plasmodium: Comprehensive phylogenetic analyses of the malaria parasites (Order Haemosporida) reveal widespread taxonomic conflict. R Soc Open Sci 5.

94. Yu G, Smith DK, Zhu H, Guan Y, Lam TT-Y. 2017. ggtree : an r package for visualization and annotation of phylogenetic trees with their covariates and other associated data. Methods Ecol Evol 8:28–36.

95. Yu G. 2020. Using ggtree to Visualize Data on Tree-Like Structures. Curr Protoc Bioinforma 69:e96.

1208 96. Katoh K, Standley DM. 2013. MAFFT Multiple Sequence Alignment Software Version
1209 7: Improvements in Performance and Usability. Mol Biol Evol 30:772–780.
1210 97. Madeira F, Park YM, Lee J, Buso N, Gur T, Madhusoodanan N, Basutkar P, Tivey ARN,
1211 Potter SC, Finn RD, Lopez R. 2019. The EMBL-EBI search and sequence analysis tools
1212 APIs in 2019. Nucleic Acids Res 47:W636–W641.
1213 98. R Core Team. 2017. R: A language and environment for statistical computing. R Found
1214 Stat Comput Vienna, Austria.
1215 99. Wickham H. 2016. Ggplot2 : elegant graphics for data analysis. Springer.
1216 100. Lin Pedersen T. 2020. patchwork, The Composer of Plots.
1217 101. Lord SJ, Velle KB, Mullins RD, Fritz-Laylin LK. 2020. SuperPlots: Communicating
1218 reproducibility and variability in cell biology. J Cell Biol 219.
1219 102. Tibúrcio M, Hitz E, Niederwieser I, Kelly G, Davies H, Doerig C, Billker O, Voss TS,
1220 Treeck M. 2021. A 39-Amino-Acid C-Terminal Truncation of GDV1 Disrupts Sexual
1221 Commitment in Plasmodium falciparum. mSphere 6.
1222 103. Eksi S, Morahan BJ, Haile Y, Furuya T, Jiang H, Ali O, Xu H, Kiattibutr K, Suri A, Czesny
1223 B, Adeyemo A, Myers TG, Sattabongkot J, Su X zhuan, Williamson KC. 2012.
1224 Plasmodium falciparum Gametocyte Development 1 (Pfgdv1) and Gametocytogenesis
1225 Early Gene Identification and Commitment to Sexual Development. PLoS Pathog 8.
1226 104. Omasits U, Ahrens CH, Müller S, Wollscheid B. 2014. Protter: Interactive protein feature
1227 visualization and integration with experimental proteomic data. Bioinformatics 30:884–
1228 886.
1229

1230 **Table S1:** Oligonucleotides **(A)** and plasmids **(B)** used in this study.

1231 **A**

| internal # | Target or Primer name | Sequence | Purpose |
|---|---|---|---|
| 284 | PF3D7_0716900 rv | GGGacgcgtTAACATCAATTTTGCTTTTTTGGG | cloning GFP-glmS |
| 285 | PF3D7_0716900 fw | GGGgcggccgctaaGGGTGTGGTAATTCAAGTACG | |
| 280 | PF3D7_0523800 rv | GGGacgcgtATTTCGTTGAATATAATTTTTTTTAATTG | |
| 281 | PF3D7_0523800 fw | GGGgcggccgctaaGTTTTCTTGTTGGTATTTTAGCTG | |
| 282 | PF3D7_0609100 rv | GGGacgcgtATGATTATGACCATGATCATGATC | |
| 283 | PF3D7_0609100 fw | GGGgcggccgctaaGGATAGCAGGTGTTACGGTTTCTTTATC | |
| 288 | PF3D7_1440800 rv | GGGacgcgtATTAGTAATAGAATTTTTCATCTTG | |
| 289 | PF3D7_1440800 fw | GGGgcggccgctaaCATTTGCTTCAAATTTGATGAG | |
| 290 | Pf3D7_1135300 rv | GGGacgcgtAGAAGTTTTTGGGGCATATTTCTTTG | |
| 338 | Pf3D7_0715900 (11) | GGGgcggccgctaaCTGGAAATAAAATAGATGGAACGTCTTG | |
| 339 | Pf3D7_0715900 (11) | GGGacgcgtAGTATCCCCTTTCAATGTGGAAC | |

| | | | |
|---|---|---|---|
| 291 | Pf3D7_1135300 fw | GGGgcggccgctaaGTTATATTATAAAAGGATGATTGG | |
| 315 | PF3D7_0523800 (1) TGD fw | GCGGCCGCTAAAGGAGCACTAAAGGCCAAAGGAAGT | cloning TGD |
| 316 | PF3D7_0523800 (1) TGD rv | acgcgtAATAATGTCATCCTTTTCATTATTAATATT | |
| 317 | PF3D7_0609100 (2) TGD fw | GCGGCCGCTAAGATTTGTTATTTGCAAAAATAATTTGTATT | |
| 318 | PF3D7_0609100 (2) TGD rv | acgcgtATGTctataaaaaaaataaatcacatac | |
| 319 | PF3D7_0716900 (3) TGD fw | GCGGCCGCTAAAAAAATGAAATTATATTTTGTACGACATTC | |
| 320 | PF3D7_0716900 (3) TGD rv | acgcgtGGCAATACCAAAGGTAATTAATAAAATTCC | |
| 323 | PF3D7_1440800 (5) TGD fw | GCGGCCGCTAAACAATGTTTAAGGATGATGAAAATAATTTT | |
| 324 | PF3D7_1440800 (5) TGD rv | acgcgtTGTATTAACAACAACTATAAATACAGAACT | |
| | Pf3D7_0715900 SLI-Tdg F | GGTGCGGCCGCGTGGATAAGATGTCGCGTTTG | |
| | Pf3D7_0715900 SLI-Tgd R | GGTACGCGTGTGTCCTACATTTTTATCATCTTCCTC | |
| | PF3D7_1135300 – fw NotI TGD | CTCGgcggccgctaaAAAAGTATGATCTCTGGAATATCCAG | |
| | PF3D7_1135300 – rv MluI TGD | TCCTacgcgtATTTATAAAGAGATCTGTTTTATTATC | |
| | PF3D7_1135300 fw NotI loxP | CTCGGCGGCCGCCCGGTAAATCTCTGGAATATCCAGCAAAATTG | cloning 1135300 loxp |
| | PF3D7_1135300 rv SpeI loxP: | TCCTACTAGTATTTATAAAGAGATCTGTTTTATTATC | |
| | PF3D7_1135300 fw AvrII loxP: | CTCGCCTAGGATGAAGTCAATGATAAGCGGTATTAG | |
| | PF3D7_1135300 rv XmaI loxP: | TCCTCCCGGGGCTTGTCTTAGGTGCGTACTTTTTAC | |
| 294 | PF3D7_0609100 int_fw | GGTAGTAACAACCTTTGGTTGTTTTATTCC | integration check PCR |
| 295 | PF3D7_0609100 int_rv | tatgtggaaggttaattaaatggacaaggg | |
| 296 | PF3D7_0716900 int_fw | GAAATTATATTTTGTACGACATTCATACTA | |
| 298 | PF3D7_1440800 int_fw | GCACAGAACATTTAAGAAGCAATGATTTTA | |
| 299 | PF3D7_1440800 int_rv | caacttgactagccaaaatgttggttctgg | |
| 300 | PF3D7_1135300 int_fw | GATCTCTGGAATATCCAGCAAAATTGTTG | |
| 302 | PF3D7_0716900 int_rv | atatttatttattttgaaccgataagctag | |
| 305 | PF3D7_1135300 int_rv | gccatatatattatacatattaaatataaagac | |
| 308 | PF3D7_0523800 int_fw | GGCCAAAGGAAGTTGGCTAACGGGGTGGTAG | |
| 309 | PF3D7_0523800 int_rv | gtgttcattcatttacctttgaatgg | |
| 369 | TGD (PF3D7_0609100 ) int check fw | atatatgttttaaagcttcaaaatg | |
| 370 | TGD (PF3D7_060 | gaggagaagcaaaaacgaaagttaac | |

| | | | |
|---|---|---|---|
| | 9100 ) int check rv | | |
| 392 | TGD (Pf3D7_0715900) int check fw | CCCACCGAAATGAACTCTTCGTTGC | |
| 393 | TGD (Pf3D7_0715900) int check rv | CTTTACCTTTAGAGGAGGAATTATTAG | |
| 394 | SLI TGD it fw Adelaide | gtggaattgtgagcggataac | |
| 327 | Pf3D7_1135300 compl | ctcgagATGAAGTCAATGATAAGCGG | cloning complementation constrcuts |
| 328 | Pf3D7_1135300 compl | cctaggGCTTGTCTTAGGTGCGTACT | |
| 553 | PKNH_0933400 fw 553 | GGGctcgagATGAAGGGAACGTACGTAG | |
| 554 | PKNH_0933400 rv 554 | GGGcctaggCACCGCCTTCGAGGCGTAC | |
| 555 | PVP01_0936100 fw 555 | GGGctcgagATGAAGGGAACGTACGTCG | |
| 556 | PVP01_0936100 rv 556 | GGGcctaggCACCGCCTTCGAGGCGTAC | |
| p37 | Pf3D7_1135300 fw 5' (TKo) | GATTTTGATATATGATTATAGGATAG | excision PCR primer |
| | Neo 40 rv | CGAATAGCCTCTCCACCCAAG | |
| | Pf3D7_1135300 fw NotI | CTCGgcggccgctaaTTATTATAAATCATATAATAAAATAAATG | cloning 1135300-2xFKBP-GFP |
| | Pf3D7_1135300 rv AvrII | TCCTcctaggAGAAGTTTTTGGGGCATATTTCTTTG | |
| 443 | Pf3D7_0715900 (11) KpnI | GggtaccAGTATCCCCTTTCAATGTGGAAC | cloning 0715900-3xHA |
| | PF3D MutOut F | GGAAATGCGGCCGCGTTACTTAAGGACGACAAAATATTCA | cloning of MutIn and MutOut |
| | PF3D MutOut R | TAAGTAACGCGGCCGCATTTCCCTTTATATTGTATTGTGCTATTGCGTTCTGTGAAAGACTAACGTACTTGTTTG | |
| | PF3D MutInqcF | tCAAGCAGCctttGCTATGGCAttccttattttctacataaagatggga | |
| | PF3D MutInqcR | CATAGCaaagGCTGCTTGaatcGCgaagtaaagaacaacgaactcta | |
| | Pf3D7_1135300 BamH I fw | cgggatccaccatgaagtcaatgataagcggtat | cloning 1135300-YFP |
| | Pf3D7_1135300 XhoI rv | CCGctcgagaccgcttgtcttaggtgcgt | |

1232

1233 **B**

| | |
|---|---|
| pSLI-*Pf*FVRT1-GFP-glmS | this study |
| pSLI-*Pf*ZIP1-GFP-glmS | this study |
| pSLI-*Pf*CDF-GFP-glmS | this study |
| pSLI-*Pf*DMT2-GFP-glmS | this study |
| pSLI-*Pf*MFS6-GFP-glmS | this study |
| pSLI-*Pf*PMRT1-GFP-glmS | this study |
| pSLI-*Pf*FVRT1-GFP-TGD | this study |
| pSLI-*Pf*ZIP1-GFP-TGD | this study |
| pSLI-*Pf*CDF-GFP-TGD | this study |
| pSLI-*Pf*DMT2-GFP-TGD | this study |
| pSLI-*Pf*MFS6-GFP-TGD | this study |

| | |
|---|---|
| pSLI-*Pf*PMRT1-GFP-TGD | this study |
| pSLI-*Pf*CDF-3xHA | this study |
| pSLI-*Pf*PMRT1-2xFKBP-GFP | this study |
| P40PX-mCherry | Jonscher et al. 2018 (40) |
| pLyn-FRB-mCherry | Birnbaum et al. 2017 (37) |
| pACP-mCherry | Birnbaum et al. 2020 (42) |
| pARL-$^{ama1}$ARO-mCherry | Cabrera et al. 2012 (44) |
| pARL-$^{ama1}$AMA1-mCherry | Wichers et al. 2021 (47) |
| pSLI-*Pf*PMRT1-loxP | this study |
| pARL-$^{nmd3}$*Pf*PMRT1-ty1 | this study |
| pARL-$^{sf3a2}$*Pf*PMRT1-ty1 | this study |
| pHcamGDV1-GFP-DD-yDHODH | this study |
| pSkip-Flox | Birnbaum et al. 2017 (37) |
| pARL- $^{nmd3}$*Pf*PMRT1-MutPV-ty1 | this study |
| pARL- $^{nmd3}$*Pf*PMRT1-MutPC-ty1 | this study |
| pARL- $^{nmd3}$*Pv*PMRT1-ty1 | this study |
| pARL- $^{nmd3}$*Pk*PMRT1-ty1 | this study |
| pGEM-*Pf*PMRT1-eYFP | this study |
| pGEM-*Pf*PMRT1-MutPV-eYFP | this study |
| pGEM-*Pf*PMRT1-MutPC-eYFP | this study |
| pGEM-SthK-eYFP | this study |

1234

Figure 1

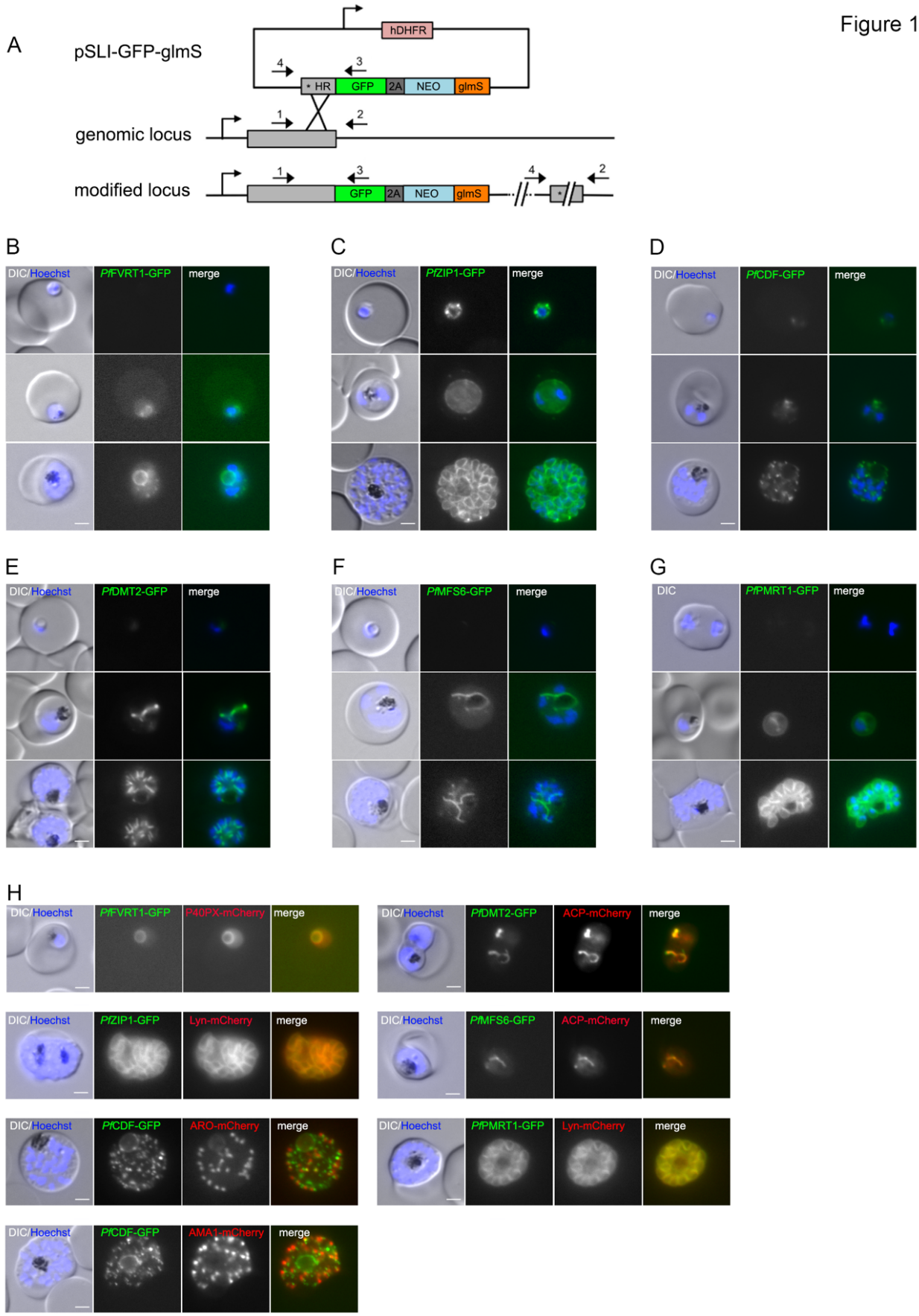

Figure 2

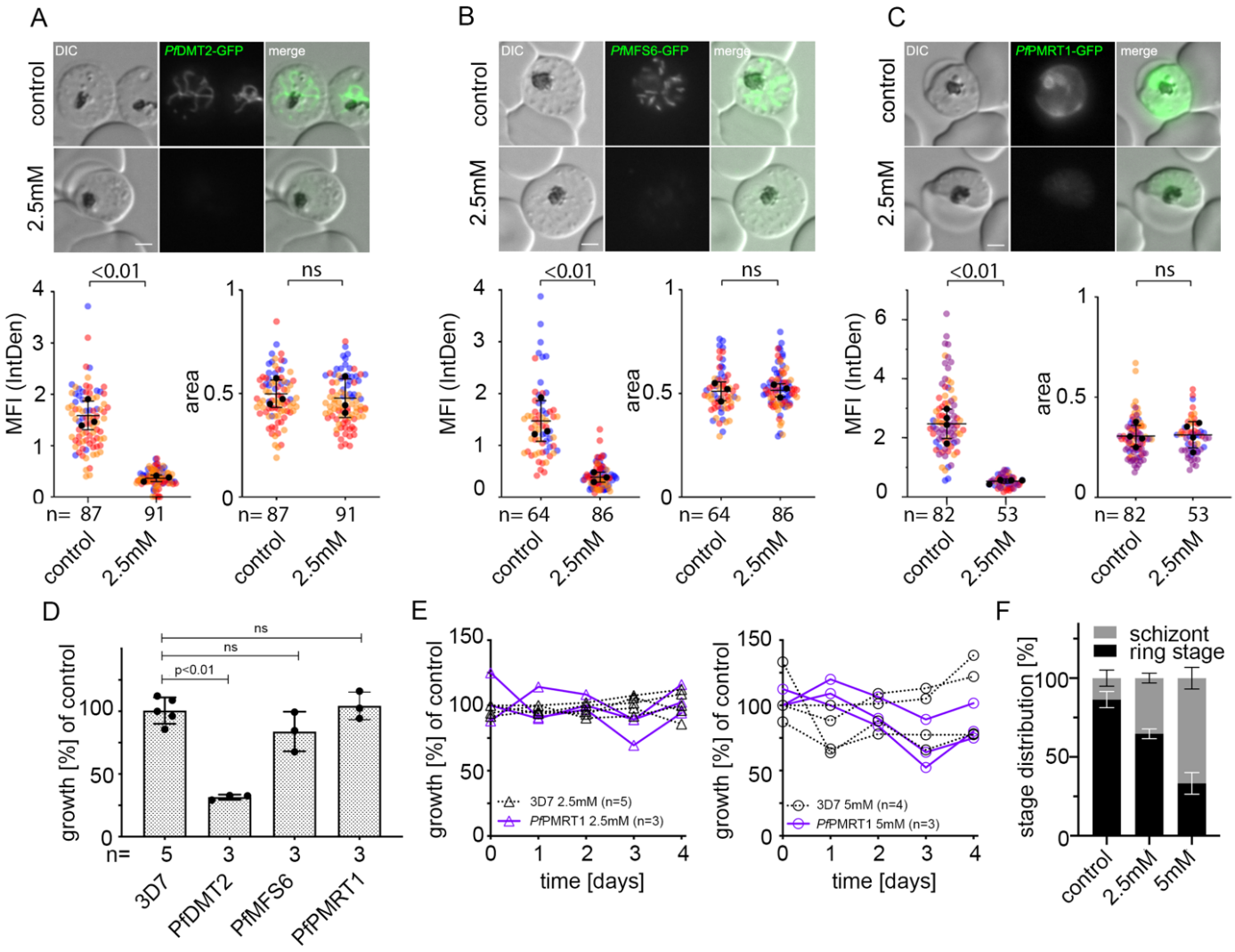

Figure 3

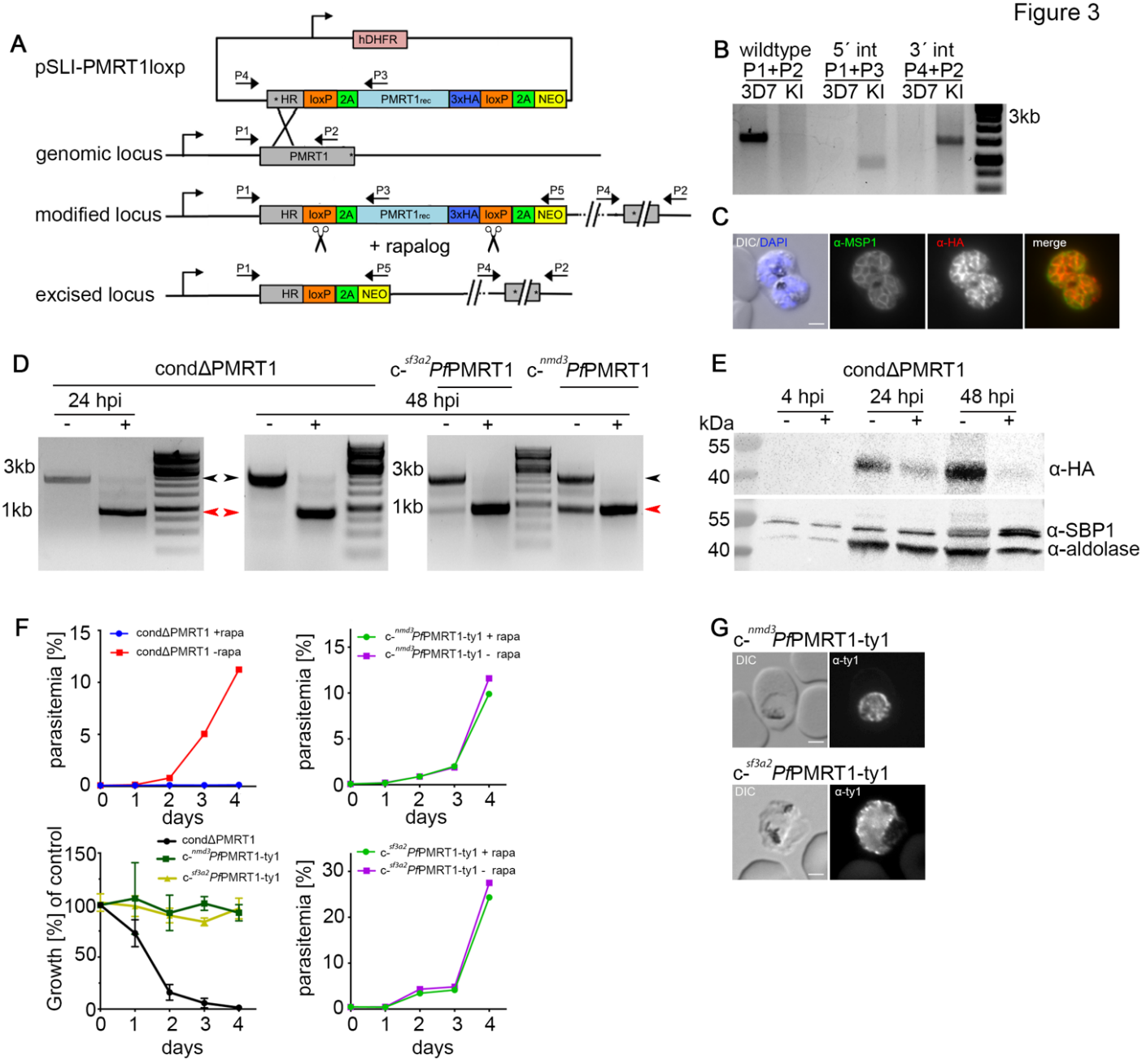

Figure 4

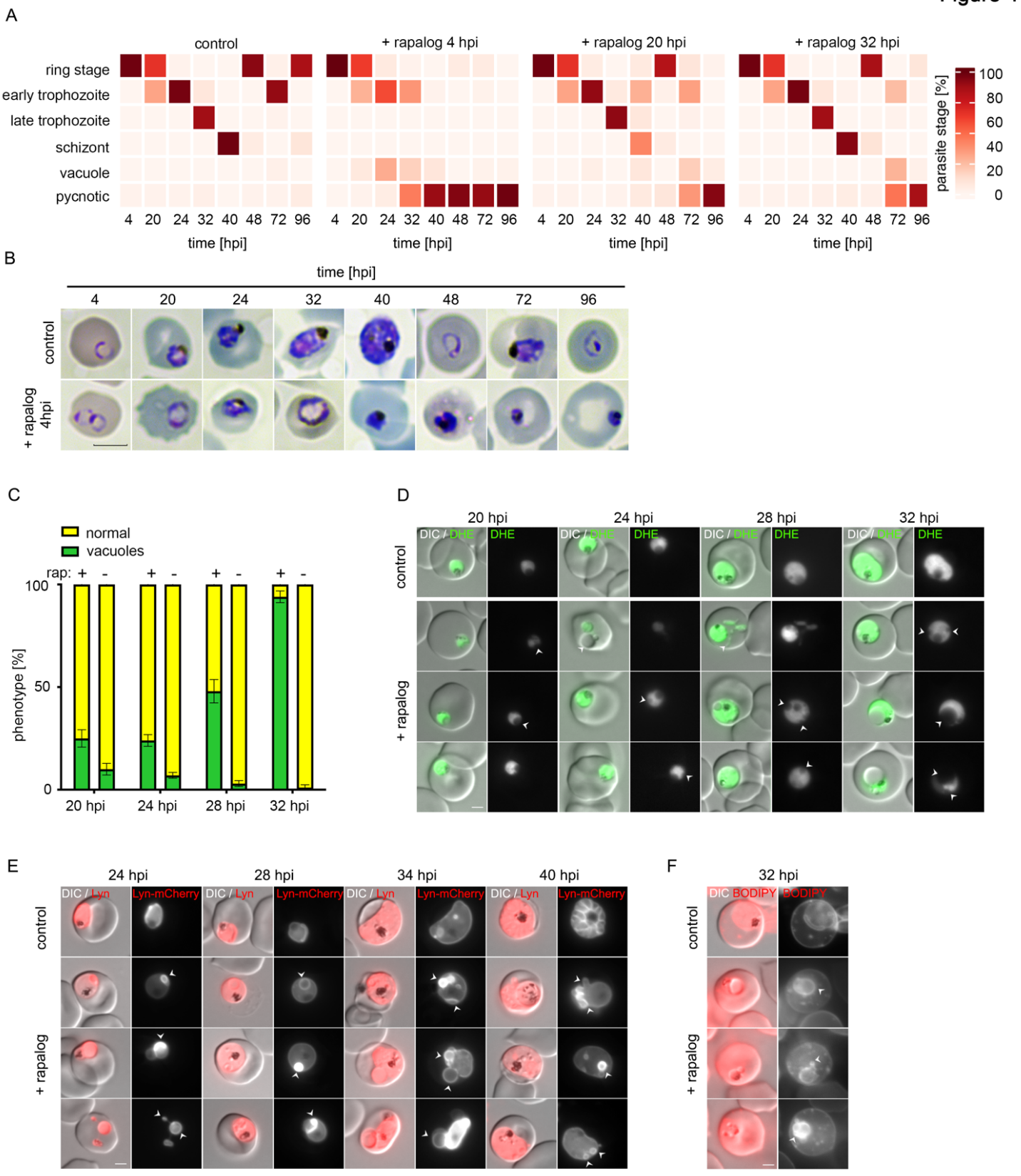

Figure 5

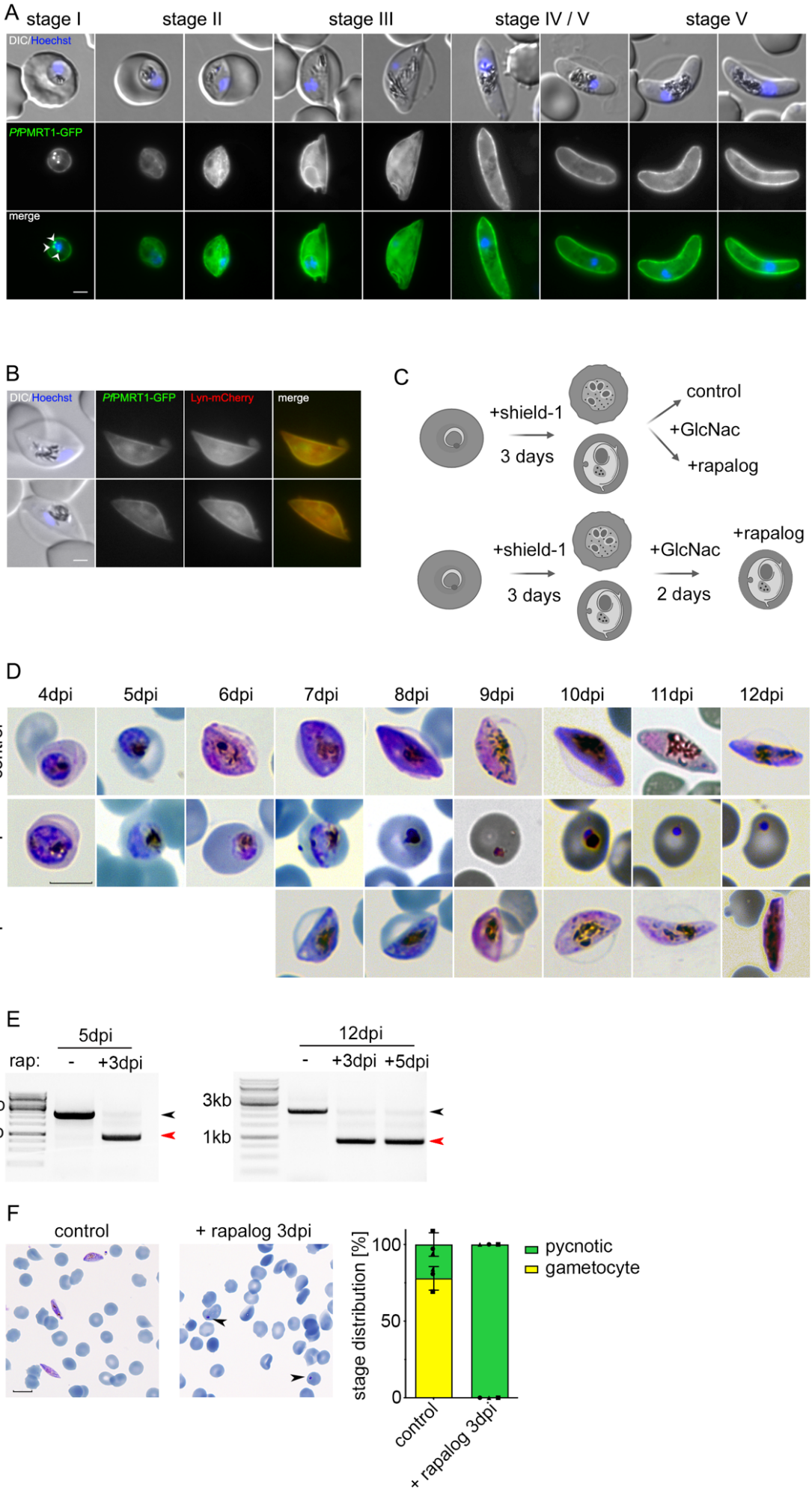

Figure 6

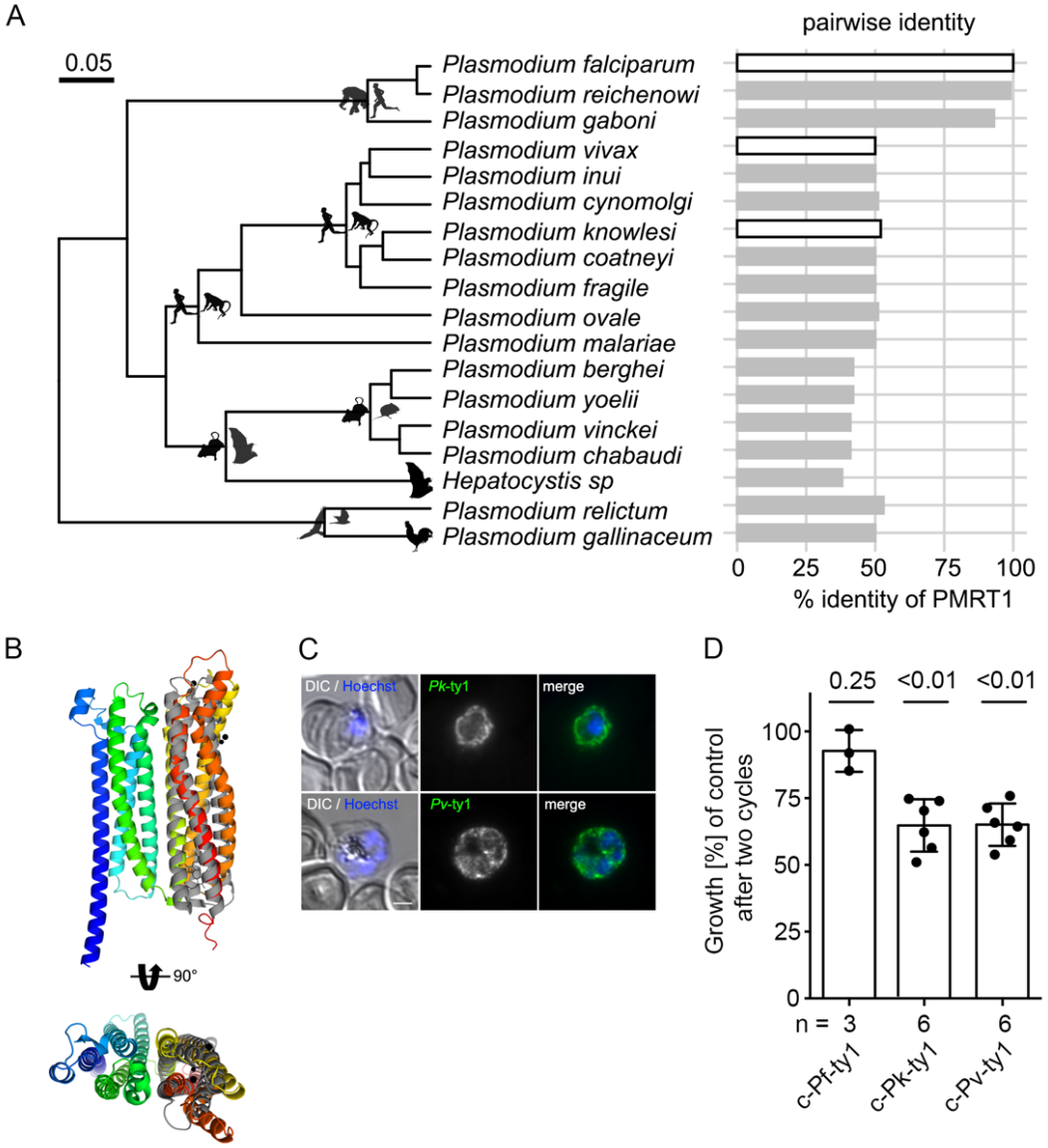

Figure 7

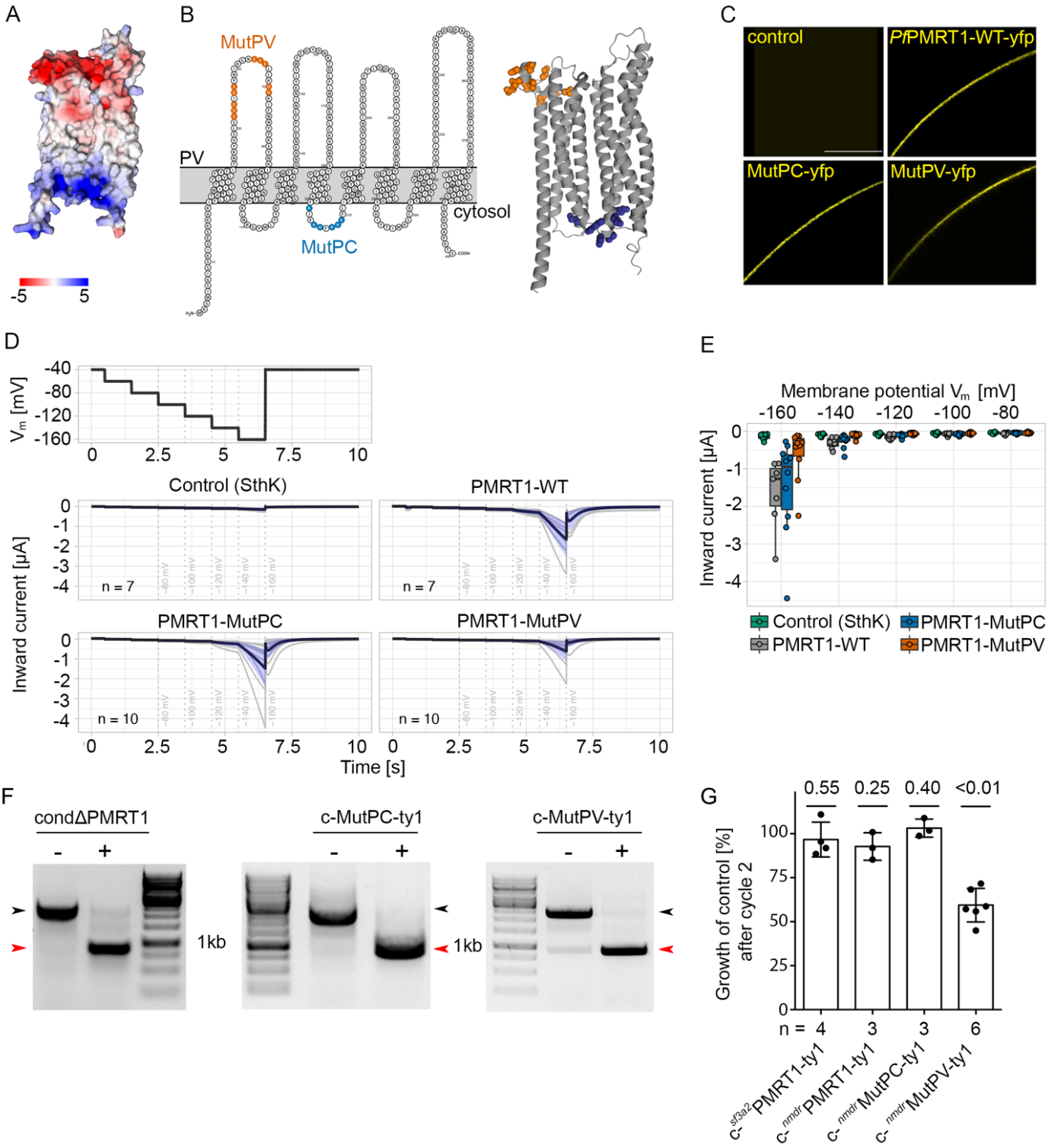

Figure S1

A

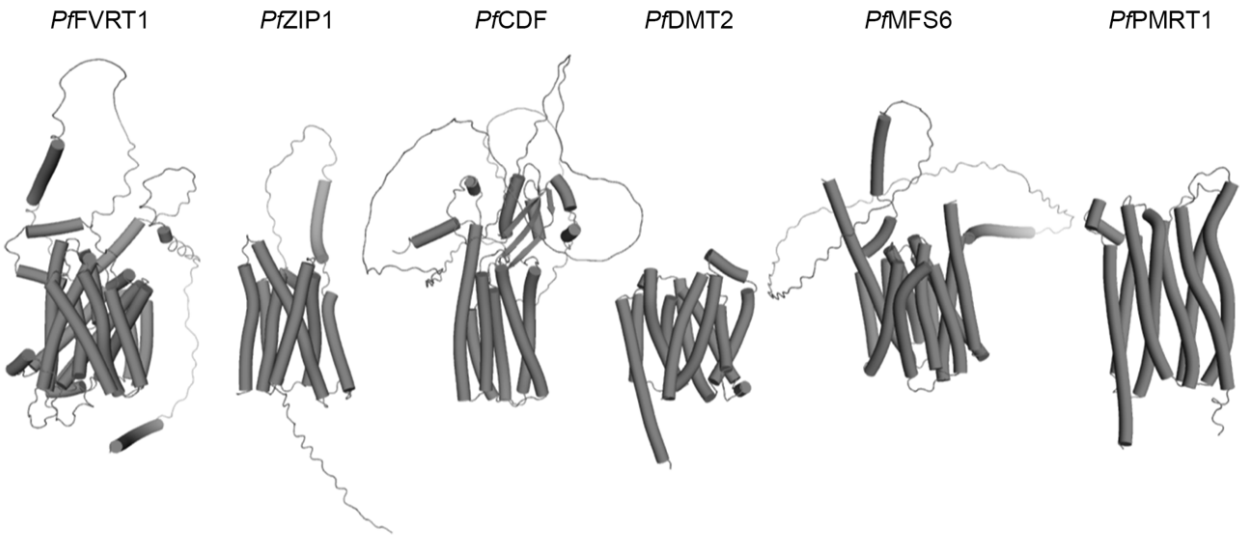


B

| | hit no. | PDB-chain | Z | msd | lali | nres | %id | PDB description on www.rcsb.org |
|---|---|---|---|---|---|---|---|---|
| *Pf*FVRT1 | 1 | 6c3i-A | 45.9 | 2.0 | 379 | 386 | 21 | Crystal structure of the Deinococcus radiodurans Nramp/MntH divalent transition metal transporter G45R mutant in an inward occluded state |
| | 2 | 5m94-A | 39.9 | 2.6 | 377 | 401 | 24 | Crystal structure of Staphylococcus capitis divalent metal ion transporter (DMT) in complex with nanobody |
| | 3 | 6tl2-A | 38.9 | 2.8 | 440 | 494 | 21 | Crystal structure of Eremococcus coleocola manganese transporter in complex with an aromatic bis-isothiourea substituted compound |
| | 4 | 6s3k-A | 25.1 | 3.8 | 357 | 573 | 8 | KimA from Bacillus subtilis in inward-facing, occluded state (APC Family Permease) |
| | 5 | 6cse-C | 24.7 | 3.4 | 344 | 428 | 13 | Crystal structure of sodium/alanine symporter AgcS with L-alanine bound |
| *Pf*ZIP1 | 1 | 6pgi-A | 16.1 | 3.6 | 206 | 230 | 15 | Asymmetric functions of a binuclear metal cluster within the transport pathway of the ZIP transition metal transporters |
| | 2 | 7c76-B | 9.5 | 3.5 | 150 | 483 | 5 | Cryo-EM structure of human TLR3 in complex with UNC93B1 |
| | 3 | 6m2l-A | 9.0 | 3.6 | 154 | 447 | 6 | Crystal structure of Plasmodium falciparum hexose transporter PfHT1 bound with C3361 |
| | 4 | 4gbz-A | 8.9 | 3.6 | 159 | 475 | 7 | The structure of the MFS (major facilitator superfamily) proton:xylose symporter XylE bound to D-glucose |
| | 5 | 6ob6-B | 8.8 | 3.6 | 155 | 357 | 12 | Human equilibrative nucleoside transporter-1, S-(4-nitrobenzyl)-6-thioinosine bound, merohedrally twinned |
| *Pf*CDF | 1 | 6xpd-B | 27.1 | 2.0 | 300 | 303 | 34 | Cryo-EM structure of human ZnT8 double mutant - D110N and D224N, determined in outward-facing conformation |
| | 2 | 3h90-C | 18.4 | 2.8 | 268 | 283 | 15 | Structural basis for the autoregulation of the zinc transporter YiiP |
| | 3 | 6vd9-A | 12.5 | 1.4 | 71 | 73 | 32 | Metal-bound C-terminal domain of the CzcD transporter from Cuprividus metallidurans |
| | 4 | 6vd8-B | 12.3 | 1.3 | 76 | 78 | 37 | Metal-bound C-terminal domain of CzcD transporter from Pseudomonas aeruginosa |
| | 5 | 3w62-A | 10.3 | 2.0 | 73 | 79 | 14 | MamM-CTD E289A |
| *Pf*DMT2 | 1 | 6ukj-A | 26.0 | 3.4 | 291 | 350 | 13 | Single-Particle Cryo-EM Structure of Plasmodium falciparum Chloroquine Resistance Transporter (PfCRT) 7G8 Isoform |
| | 2 | 5ogk-E | 24.9 | 3.6 | 285 | 298 | 14 | Crystal structure of a nucleotide sugar transporter with bound nucleotide sugar |
| | 3 | 6xbo-A | 24.6 | 3.8 | 275 | 319 | 12 | X-ray crystal structure of the mouse CMP-Sialic acid transporter in complex with 5-methyl CMP |
| | 4 | 5i20-D | 24.0 | 3.1 | 272 | 280 | 9 | Crystal structure of protein (drug metabolite transporter YddG) |
| | 5 | 5y78-A | 23.9 | 4.0 | 288 | 305 | 14 | Crystal structure of the triose-phosphate/phosphate translocator in complex with inorganic phosphate |
| *Pf*MFS6 | 1 | 6t1z-A | 36.6 | 3.0 | 366 | 393 | 15 | LmrP from L. lactis, in an outward-open conformation, bound to Hoechst 33342 |
| | 2 | 6s4m-A | 36.1 | 2.3 | 356 | 426 | 17 | Crystal structure of the human organic anion transporter MFSD10 (TETRAN) |
| | 3 | 3wdo-A | 35.7 | 3.1 | 364 | 453 | 12 | Structure of E. coli YajR transporter |
| | 4 | 3o7p-A | 35.2 | 3.0 | 356 | 410 | 11 | Crystal structure of the E.coli Fucose:proton symporter, FucP (N162A) |
| | 5 | 7ckr-A | 35.0 | 2.7 | 365 | 382 | 7 | Cryo-EM structure of the human MCT1/Basigin-2 complex in the presence of anti-cancer drug candidate BAY-8002 in the outward-open conformation |
| *Pf*PMRT1 | 1 | 6z0c-A | 15.5 | 3.3 | 169 | 199 | 4 | Structure of in silico modelled artificial Maquette-3 protein |
| | 2 | 5vjt-A | 14.9 | 3.3 | 171 | 196 | 3 | De Novo Photosynthetic Reaction Center Protein Equipped with Heme B and Zn(II) cations |
| | 3 | 7p5c-B | 12.7 | 3.2 | 153 | 392 | 4 | Cryo-EM structure of human TTYH3 in Ca2+ and GDN (Protein Tweety Homolog 3) |
| | 4 | 6njm-E | 12.5 | 2.0 | 116 | 117 | 0 | Architecture and subunit arrangement of native AMPA receptors (Glutamate-gated AMPA receptor) |
| | 5 | 6y90-A | 12.0 | 3.5 | 140 | 172 | 8 | Structure of full-length CD20 in complex with Rituximab Fab (B-Lymphocyte Antigen CD20) |

Dali Z score: significance estimate

msd: difference between the rmsd value associated with a protein structure pair and the rmsd value that would have been observed in the case that the two structures had the same crystallographic resolution

lali: number of aligned positions

nres: number of residues in the matched structure

%id: the percentage sequence identity in the match

rmsd: root-mean-square-deviation over aligned α-carbon position

Figure S2

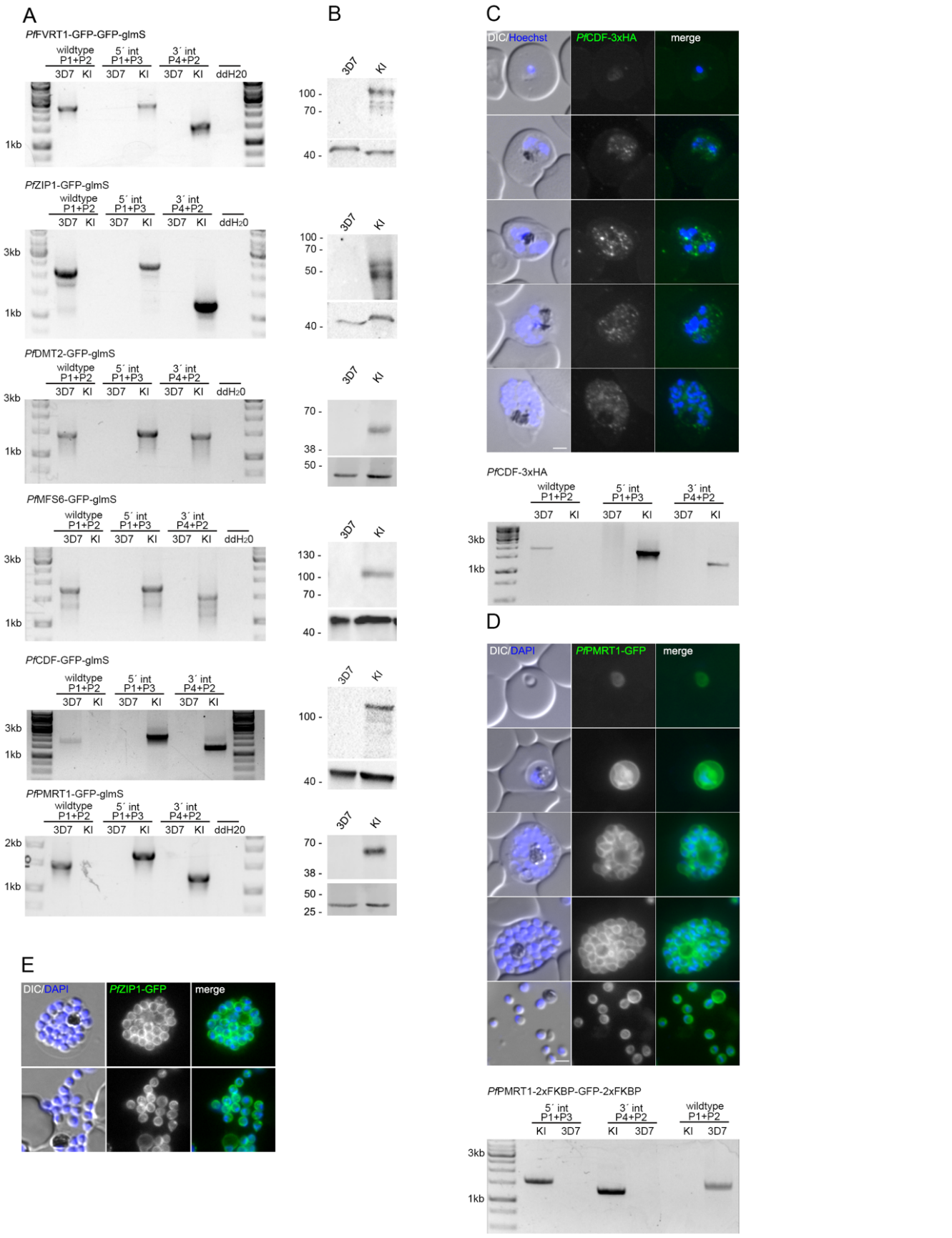

Figure S3

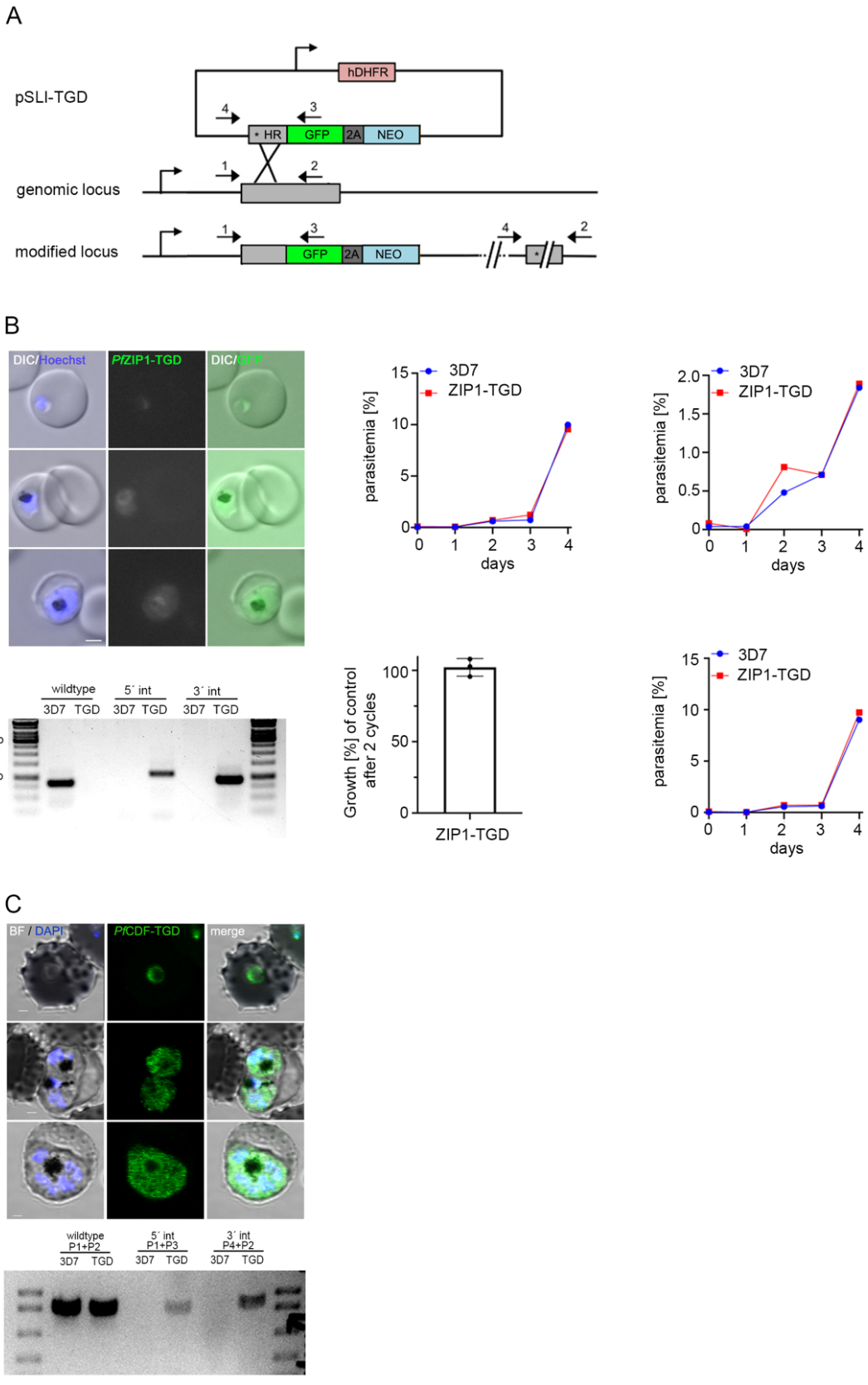

Figure S4

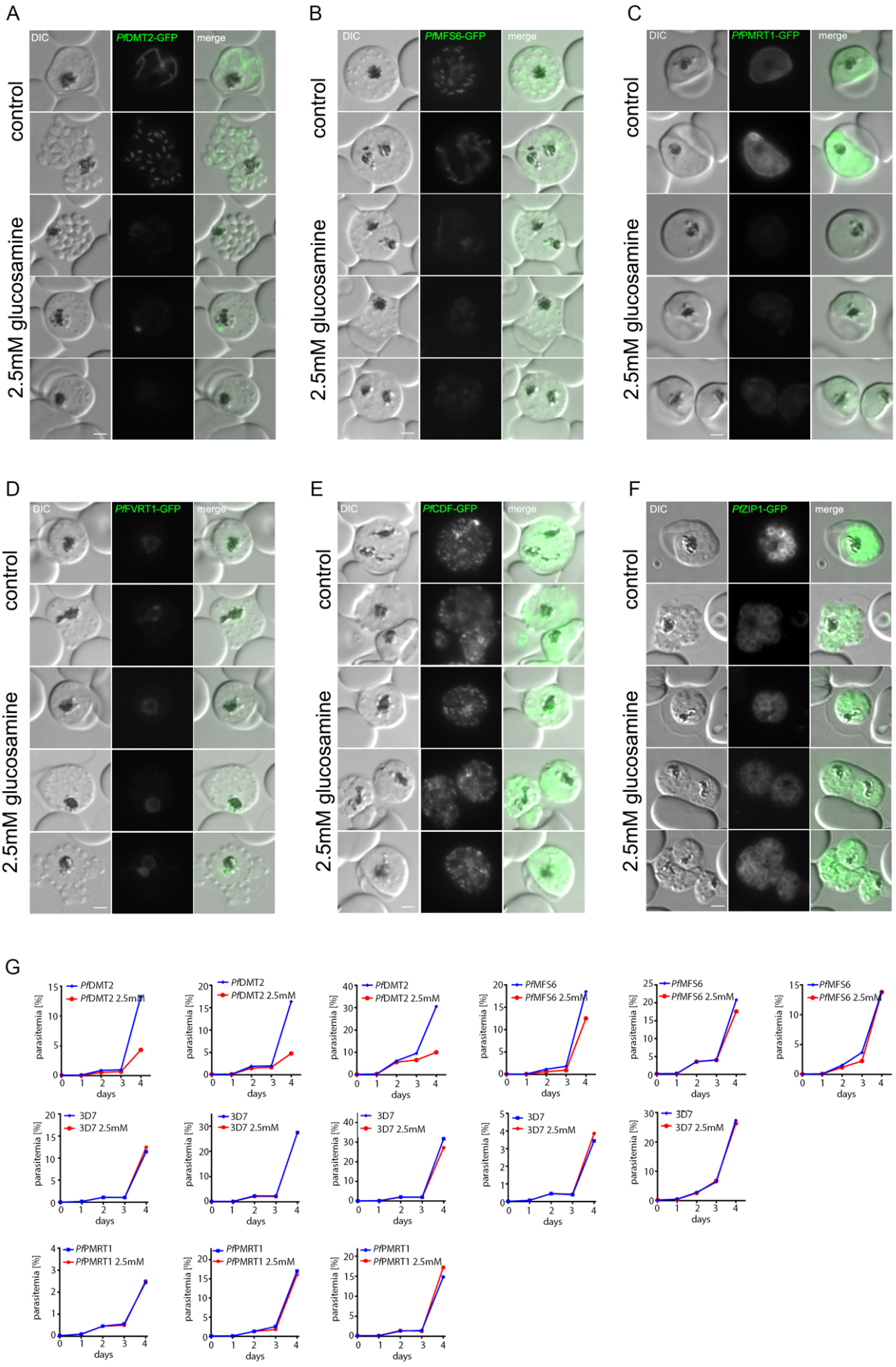

# Figure S5

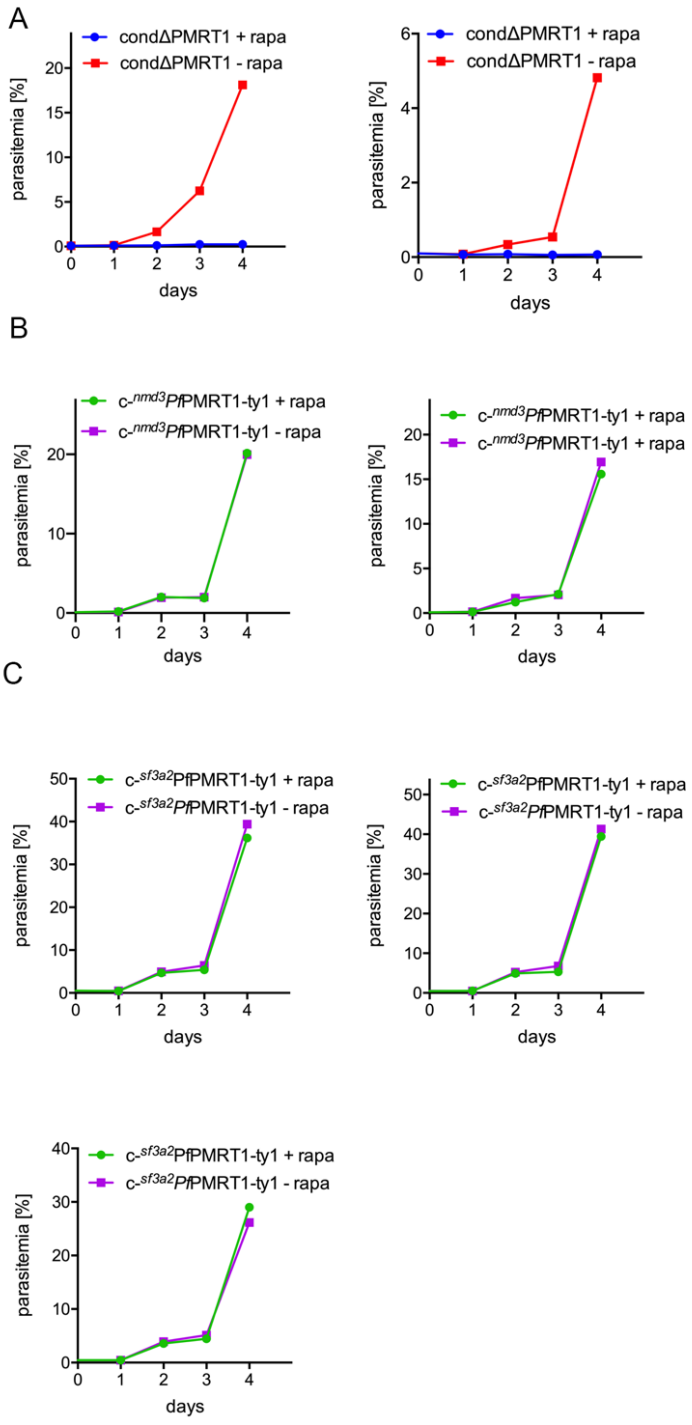

Figure S6

A

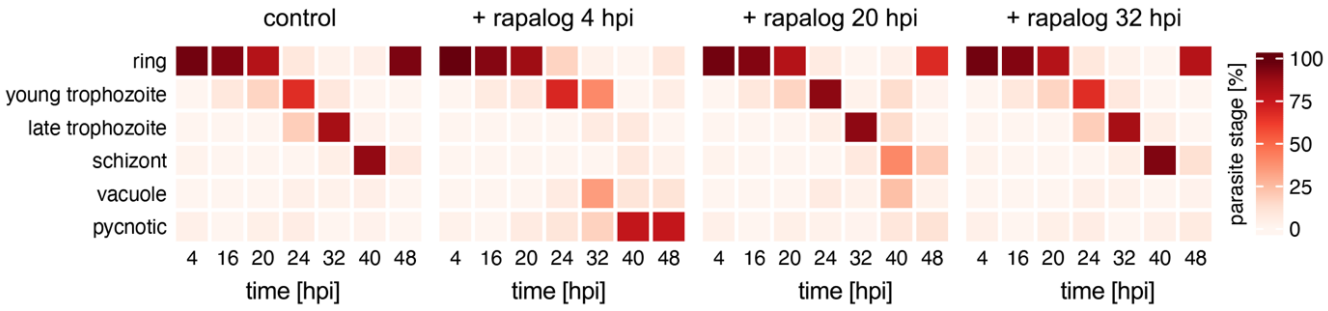


B

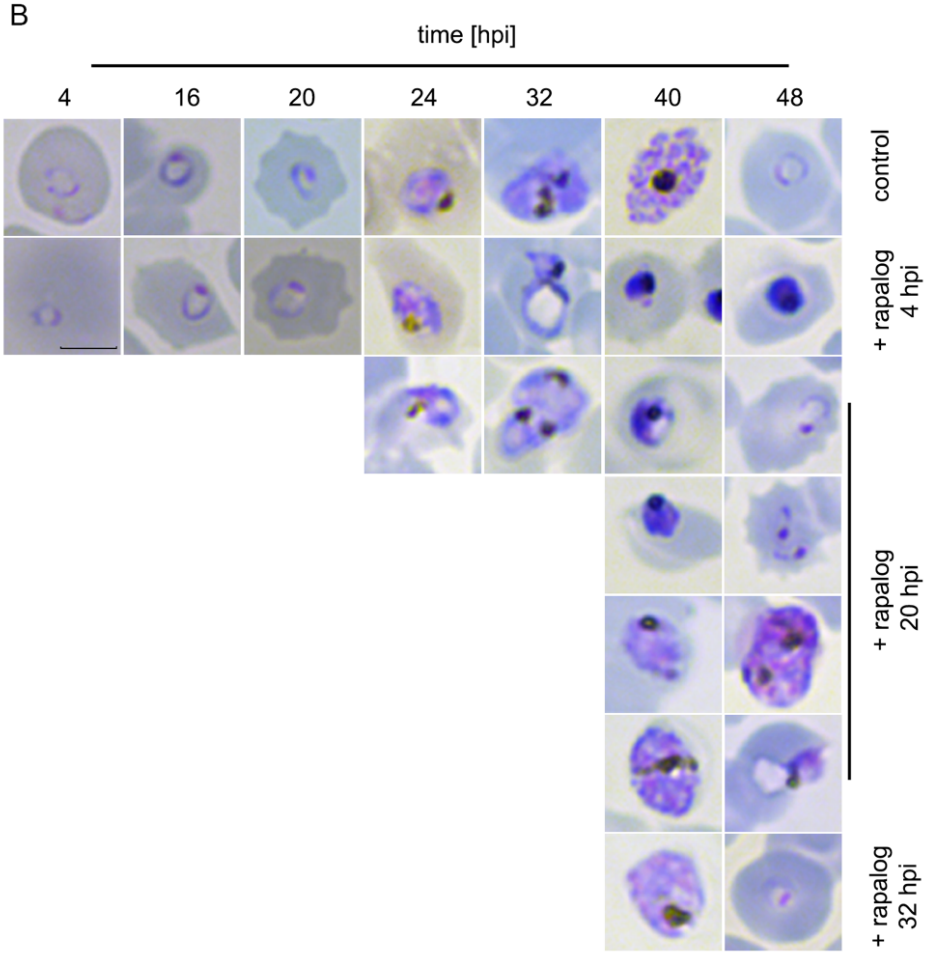

Figure S7

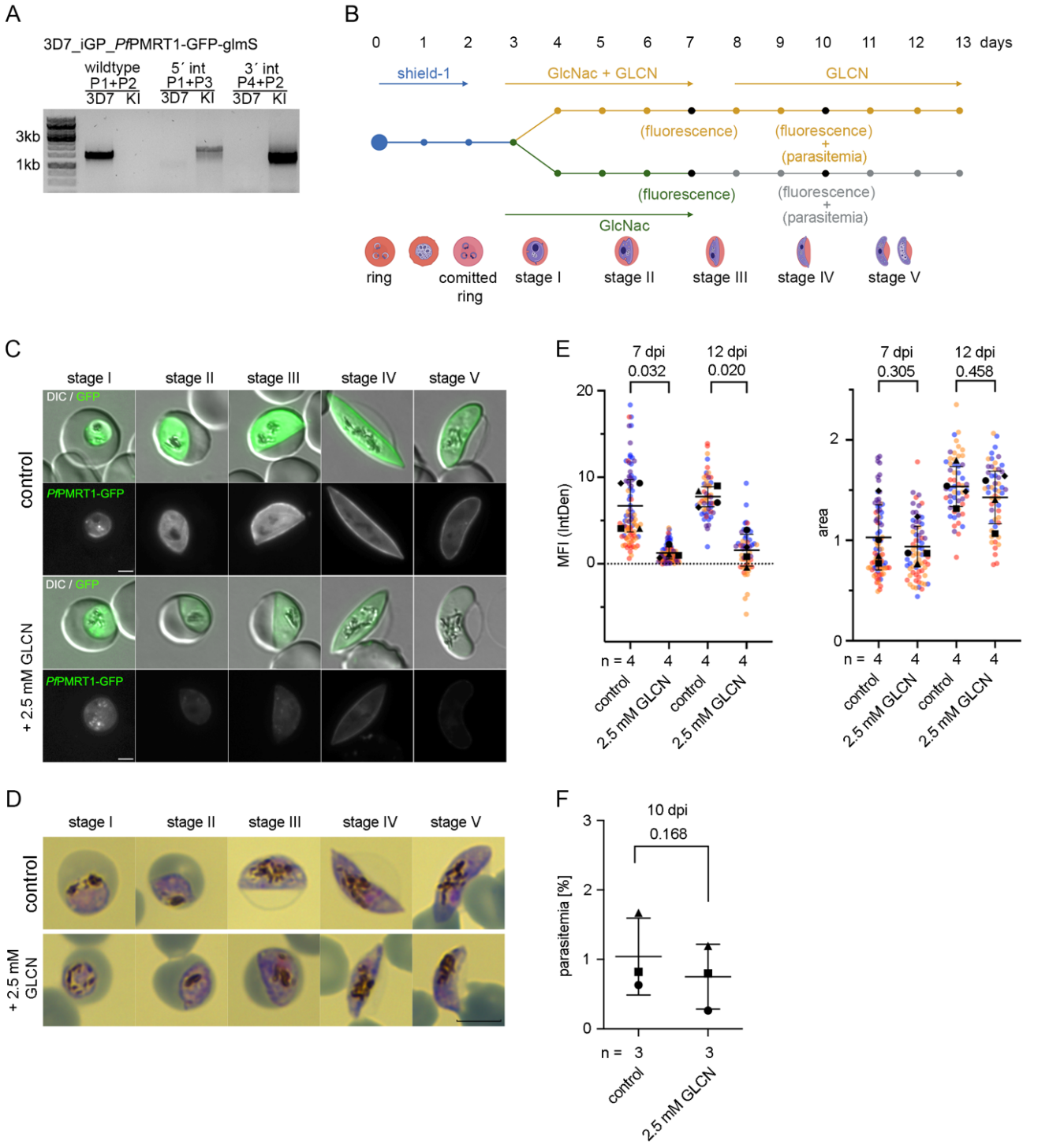

Figure S8

A

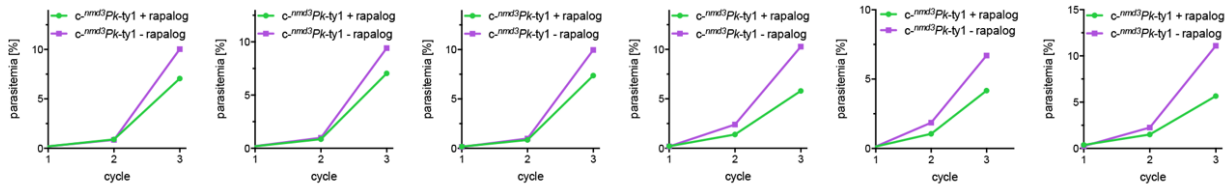


B

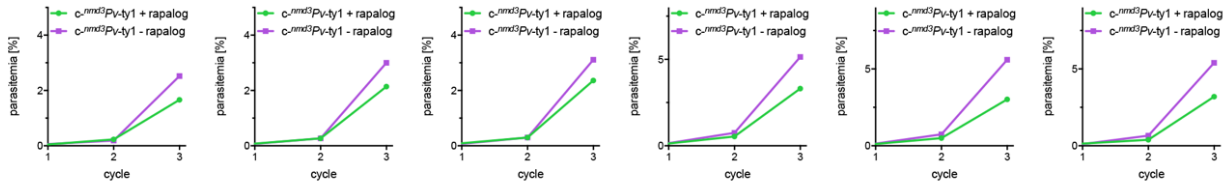

Figure S9